



HAL
open science

Extension modes and breakup processes of the southeast China-Northwest Palawan conjugate rifted margins

Michael Nirrengarten, G. Mohn, N.J. Kuszniir, F. Sapin, F. Despinois, M.
Pubellier, S.P. Chang, H.C. Larsen, J.C. Ringenbach

► To cite this version:

Michael Nirrengarten, G. Mohn, N.J. Kuszniir, F. Sapin, F. Despinois, et al.. Extension modes and breakup processes of the southeast China-Northwest Palawan conjugate rifted margins. *Marine and Petroleum Geology*, 2020, 113, pp.104123. 10.1016/j.marpetgeo.2019.104123 . hal-02778748

HAL Id: hal-02778748

<https://hal.science/hal-02778748>

Submitted on 21 Jul 2022

HAL is a multi-disciplinary open access archive for the deposit and dissemination of scientific research documents, whether they are published or not. The documents may come from teaching and research institutions in France or abroad, or from public or private research centers.

L'archive ouverte pluridisciplinaire **HAL**, est destinée au dépôt et à la diffusion de documents scientifiques de niveau recherche, publiés ou non, émanant des établissements d'enseignement et de recherche français ou étrangers, des laboratoires publics ou privés.



Distributed under a Creative Commons Attribution - NonCommercial 4.0 International License

1 **Extension modes and breakup processes of the Southeast China-** 2 **Northwest Palawan conjugate rifted margins**

3 *Nirrengarten M.^{1*}, Mohn G.¹, Kuszniir N.J.², Sapin F.³, Despinois F.³, Pubellier*
4 *M.⁴, Chang S.P.⁴, Larsen H.C.^{5,6}, Ringenbach J.C.³*

5
6 *¹ Département Géosciences et Environnement, Université de Cergy-Pontoise, Cergy-*
7 *Pontoise, France*

8 *² Department of Earth and Ocean Sciences, University of Liverpool, Liverpool, UK*

9 *³ Total SA, CSTJF, Pau, France*

10 *⁴ Laboratoire de Géologie, UMR 8538, École Normale Supérieure, CNRS, Paris, France*

11 *⁵ State Key Laboratory of Marine Geology, Tongji University, Shanghai, China.*

12 *⁶ Geological Survey of Denmark and Greenland, Copenhagen, Denmark*

13
14 ***Corresponding author:**

15 Michael Nirrengarten

16 michael.nirrengarten@u-cergy.fr

17 Laboratoire GEC, Université de Cergy Pontoise

18 1 rue Descartes

19 95000 Neuville-sur-Oise, France

20

21 **Keywords:** Conjugate rifted margins; South China Sea breakup; IODP Expedition 367-368;
22 Gravity modelling

23 **Abstract:**

24 Our understanding of continent-ocean transition structures and magmatism in the absence
25 of excessive magmatic additions has been guided by the observations and models developed
26 at the magma-poor Iberia-Newfoundland conjugate margins. Recently these models have
27 been challenged in the South China Sea in light of new IODP Expeditions 367-368-368X. We
28 have used an integrated analysis of high quality seismic reflection and gravity anomaly data,
29 calibrated against recent deep sea drilling results, to investigate margin structure and
30 tectono-magmatic interplay during continental breakup and early seafloor spreading
31 between the SE China-NW Palawan conjugate margins.

32 The Eocene-Oligocene South China Sea rifting initiates in a heterogeneous and likely
33 thermally un-equilibrated lithosphere formed by the Mesozoic Yenshanian orogeny. Gravity
34 and joint inversion methods confirm lateral variation of basement densities across the
35 conjugate margins. Lithospheric and basement heterogeneities induced a rifting style
36 characterized by a series of highly thinned rift basins associated with extensional faulting

37 soling out at various crustal levels. Final rifting in late Eocene triggered decompression
38 melting forming mid-ocean ridge type magmatism, which emplaced within thinned
39 continental crust as deep intrusions and shallow extrusive rocks. This initial magmatic
40 activity was concomitant with continued deformation of continental crust by extensional
41 faulting. Integrated analysis of seismic reflection profiles and gravity anomaly data combined
42 with deep-sea boreholes accurately locate the continent-ocean boundary. We show that the
43 initial igneous crust, continentward of oceanic magnetic anomaly C10n, is asymmetric in
44 width and in morphology for the conjugate margins. The wider and faulted newly accreted
45 domain on the SE China side indicates that magmatic accretion is associated with tectonic
46 faulting during the formation of initial oceanic lithosphere. We suggest that deformation was
47 not symmetrically distributed between the conjugate margins during the initiation of
48 seafloor spreading but evolved asymmetrically until the stabilisation of the spreading ocean
49 ridge around C10n. The analysis of the South China Sea breakup reveals a transient interplay
50 between faulting, magmatic budget and extension rates during the formation of the
51 continent-ocean transition and initial emplacement of igneous crust.

52

53 **1. Introduction**

54 Rifting processes may result in continental breakup through the extension and thinning of
55 continental lithosphere. Continental breakup mechanisms are recorded within the
56 Continent-Ocean Transition (COT) of passive margins where continental extension evolves
57 into localized accretion of new oceanic lithosphere (Dewey and Bird, 1970; Falvey, 1974;
58 Heezen, 1960; McKenzie, 1978; Whitmarsh et al., 2001). Such mechanisms are by definition
59 transient and characterized by complex tectono-magmatic interplays evolving through time
60 and operating on inherited heterogeneous lithosphere (e.g. Petri et al., 2019; Reston, 2009;
61 Taylor et al., 1999). Seismic images of rifted margins show large variability of COT
62 architectures indicating different tectono-magmatic processes. Extensional structures
63 interpreted in the COT such as high angle normal or low angle extensional faults depend on
64 the rheological inheritance and evolution of the crust and underlying mantle during rifting
65 (e.g. crustal embrittlement (Pérez-Gussinyé et al., 2003), and lower crustal ductility (Brune et
66 al., 2017; Clerc et al., 2018, 2015; Huisman and Beaumont, 2011). In general, extension and
67 lithospheric thinning trigger decompression melting and Mid-Ocean Ridge Basalt (MORB)
68 type magmatism at COTs (McKenzie and Bickle, 1988). Timing, volume and localization of
69 this magmatism are highly variable in the COT and are controlled among others by extension
70 rate, initial lithosphere geotherm, crustal rheology, initial crustal thickness and inheritance
71 (Davis and Lavier, 2017). In that context, when analysing the development of rifted margins
72 from rift initiation to the stable accretion of an oceanic lithosphere, it is fundamental to
73 address the timing and relative importance of tectonic and magmatic processes, including
74 symmetric or asymmetric evolution of paired conjugate margins. As already identified in the
75 80s by the IPOD (International Phase of Ocean Drilling) program on passive continental
76 margins (Curry, 1980), without drilling data, the interplay in time and space between
77 crustal deformation, lithospheric thinning and magmatism remains unresolved.

78 In that perspective, the South China Sea (SCS) rifted margins represent a key natural
79 laboratory benefiting from extensive long offset seismic reflection and refraction profiles
80 (e.g. Gao et al., 2015; Pichot et al., 2014; Pin et al., 2001; Yang et al., 2018; Lei and Ren,
81 2016) in combination with borehole data (Larsen et al., 2018e; Li et al., 2015) from both
82 academic and industrial surveys. The rifted continental domain leading to the formation of
83 the SCS oceanic domain is remarkably wide (>600 km cumulated over both conjugate

84 margins), but is not equally distributed between the SE China and the NW Palawan
85 conjugate margins (Fig. 1). Results from the recent IODP (International Ocean Discovery
86 Program) Expeditions 367-368-368X, with six boreholes drilling the acoustic basement on the
87 ~400 km wide SE China (Larsen et al., 2018d), revealed the presence in its distal parts of a
88 sharp transition from thinned continental crust to igneous crust. This contrasts markedly
89 with the only other extensively drilled COT, the North Atlantic magma-poor Iberia-
90 Newfoundland margins, where large domains (>100 km) of exhumed continental lithospheric
91 mantle have been sampled by drilling on both conjugate margins (Boillot et al., 1987;
92 Tucholke and Sibuet, 2007; Whitmarsh et al., 1996; Whitmarsh and Wallace, 2001). The
93 evolution of the SE China margin COT and initial seafloor spreading, however, have not been
94 yet fully integrated with that of its conjugate NW Palawan margin.

95 Therefore, this contribution, combining available geological and geophysical datasets, aims
96 to analyse the nature and architecture of the SE China-NW Palawan conjugate margins to
97 assess the interactions between extension, faulting and magmatic additions during breakup
98 and early stages of oceanic accretion. We use reflection seismic lines on both the distal SE
99 China and NW Palawan margins combined with 3D free-air gravity anomaly inversion to
100 determine their crustal architectures. In addition, we have performed joint inversion of
101 seismic reflection and gravity anomaly data. This allows us to determine crustal thickness
102 and crustal density variations reflecting structural and crustal domain boundaries on a
103 regional scale. The IODP drilling results offer critical local constraints on basement nature
104 and on the timing of rifting and breakup. The SE China-NW Palawan conjugate margins
105 presents a scenario of late rifting and breakup evolution that differs from other drilled
106 conjugate systems (Iberia-Newfoundland (Mohn et al., 2015; Tucholke et al., 2007)

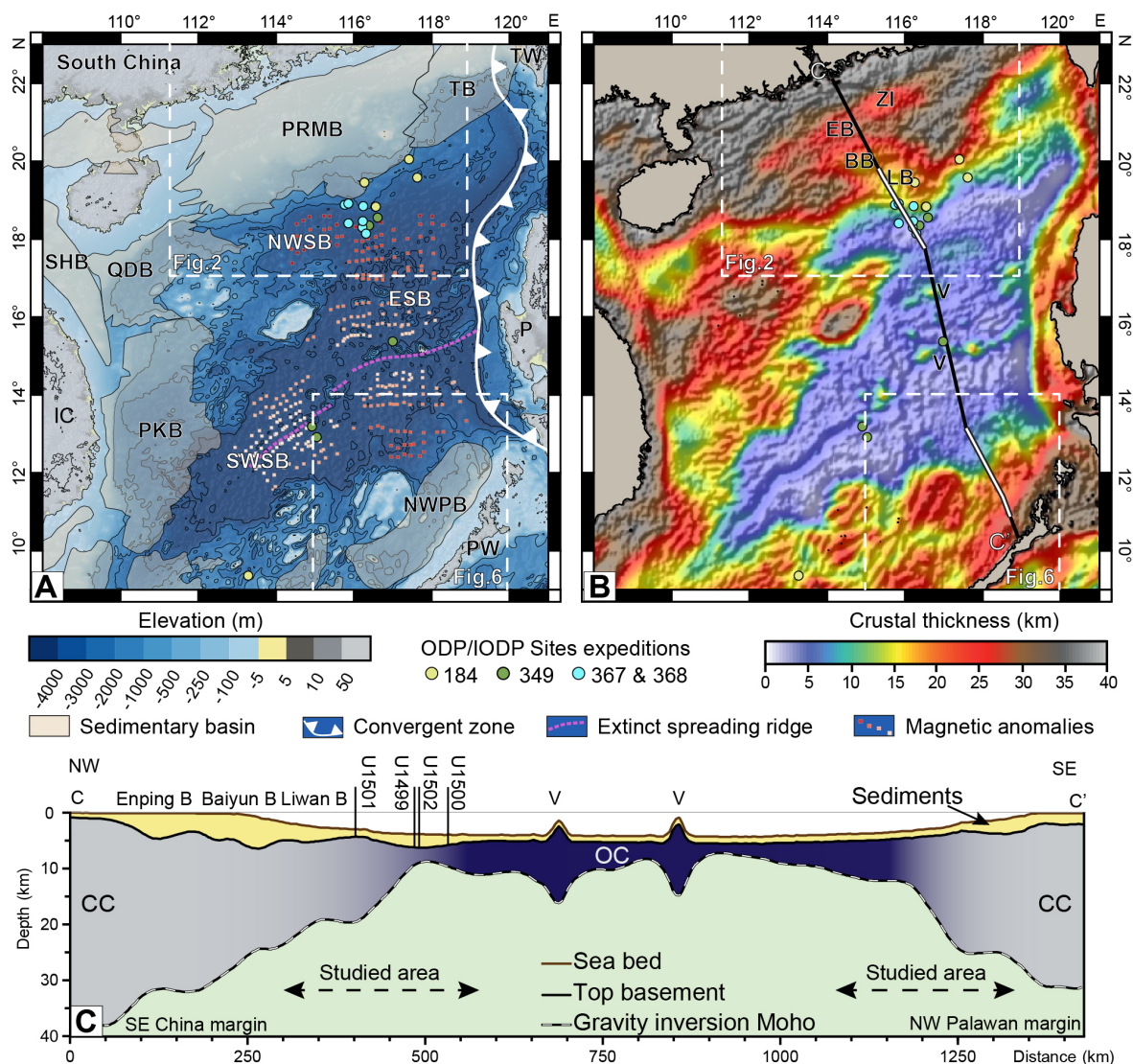
107

108 **2. Geological setting**

109 **2.1) South China Sea tectonic evolution**

110 The SCS is a south-westward oriented V-shaped oceanic basin (~1200 km long and a
111 maximum width of ~800km) of Oligocene to mid Miocene age (Fig. 1, Briaies et al., 1993;
112 Taylor and Hayes, 1983). The eastern part of SCS oceanic lithosphere is currently subducting
113 beneath the Manila Trench to the East. Initiation of this subduction zone started likely in
114 early Miocene (Arfai et al., 2011; de Boer et al., 1980) contemporaneously with the cessation

115 of the SCS spreading (Franke et al., 2014) and with large left-lateral movement of the
 116 Philippines Islands toward the north. This motion is interpreted as related to the northward
 117 drift of the Australia plate that strongly deformed the eastern border of the Sunda Plate
 118 during the Neogene (Pubellier et al., 2003). Variable ages for seafloor spreading cessation
 119 were proposed based on oceanic magnetic anomaly modelling (20.5 Ma (Barckhausen et al.,
 120 2014), 15.5 Ma (Briais et al., 1993) or 15 Ma (C.-F. Li et al., 2014)). The SCS oceanic domain
 121 can be divided into three well defined segments (Eastern, Northwestern and Southwestern
 122 sub-basins) (Fig. 1) reflecting spreading axis jumps and changes in spreading ridge
 123 orientation (Briais et al., 1993; Sibuet et al., 2016) as well as a propagation of breakup
 124 toward the southwest.



125
 126 **Figure 1: A) Topographic map of the SCS (Amante & Eakins, 2009) associated with the oceanic**
 127 **magnetic anomalies (Briais et al., 1993) B) Crustal thickness map determined by 3D gravity**

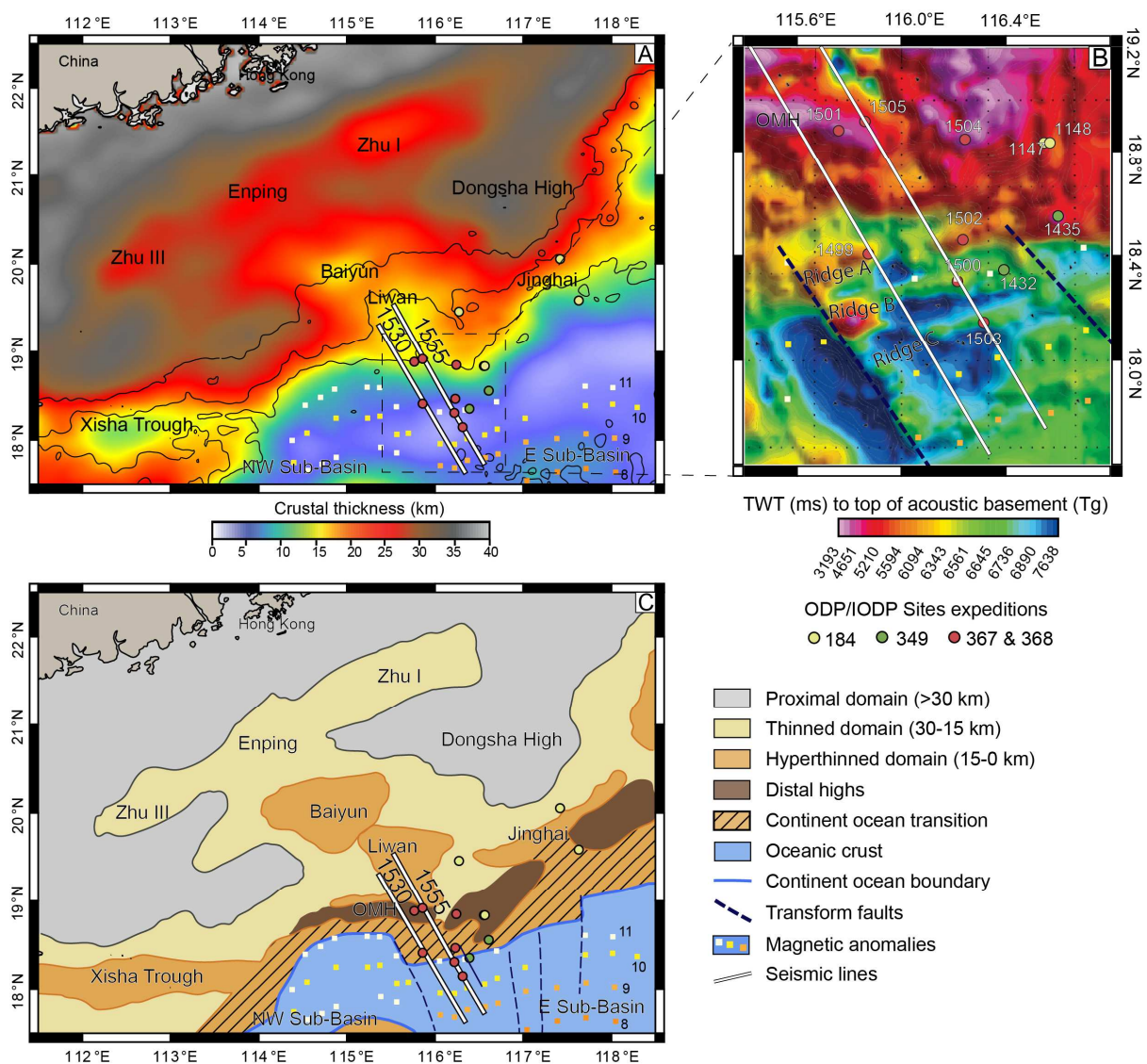
128 anomaly inversion with the free-air gravity anomaly in shaded relief (Gozzard et al., 2019) and the
129 location of profile C C) Profile extracted from the crustal thickness map determined by 3D gravity
130 anomaly inversion (Gozzard et al., 2019) crossing the SCS from SE China to NW Palawan coast. BB:
131 Baiyun Basin, CC: Continental Crust EP: Enping Sub-Basin, ESB: East sub-basin IC: Indochina, QB:
132 Qiongdongnan Basin, LB: Liwan Sub-Basin, NWPB: Northwest Palawan Basin, NWSB: Northwestern
133 Sub-Basin, OC: Oceanic crust, P: Philippines, PKB: Phu Khan Basin, PRMB: Pearl River Mouth Basin,
134 PW: Palawan, SHB: Song Hong-Yinggehai Basin, SWSB: Southwest Sub-Basin, TB: Tainan Basin, TW:
135 Taiwan, V: Volcano, ZI: Zhu I Basin

136

137 The oldest oceanic crust has been dated by magnetic modelling at 33-32 Ma in the
138 Eastern oceanic sub-basin (Briais et al., 1993; Taylor and Hayes, 1983). The initial N-S
139 direction of SCS spreading continued up to the C6b anomaly (~23 Ma) and is limited to the
140 Eastern and Northwestern sub-basins. Afterward, spreading migrated from NE to SW
141 between ~23 and ~16 Ma and formed the Southwestern sub-basin (Briais et al., 1993; Zhou
142 et al., 1995). This propagation of deformation caused each margin segment to have its own
143 major rifting event and breakup history (Franke et al., 2014; Savva et al., 2014). The
144 variations in the propagation velocity and orientation have been recently interpreted as
145 resulting from out of plane compression forces (Le Pourhiet et al., 2018), that might be
146 caused by continental lithosphere masses reorganisation during Himalayan growth and
147 kinematic reorganisation.

148 Rifting of the SCS continental lithosphere occurred in a very wide domain (>600 km)
149 characterised by several thick sedimentary basins (e.g. Pearl River Mouth (PRMB), Phuh
150 Khan, Tainan) (Hayes and Nissen, 2005; Ru and Pigott, 1986) (Figs. 1, 2). The age of initial
151 rifting in the SCS is not fully resolved. Most of the industry boreholes across the sedimentary
152 basins on the proximal margin are located on basement highs and record condensed
153 continental facies, whose dates from palynology are only poorly resolved. In the Eastern sub-
154 basin, ages of rifting are mainly based on the evolution of the PRMB. This basin shows
155 evidence for two phases of extension preceding continental breakup, one of Late Cretaceous
156 to early Paleocene age and a second of middle Eocene to early Oligocene age (Ru and Pigott,
157 1986; Zhou et al., 1995). The first Late Cretaceous to early Paleocene rift event is associated
158 with the deposition of the Shenhu Formation characterized by continental clastic
159 sedimentation containing many metamorphic and volcanic fragments (Sizhong and Cunmin,

160 1993; Zhou et al., 1995) (Fig. 3). This event is associated to the post-orogenic dismantling of
 161 the Yenshanian Arc (Klimetz, 1983).



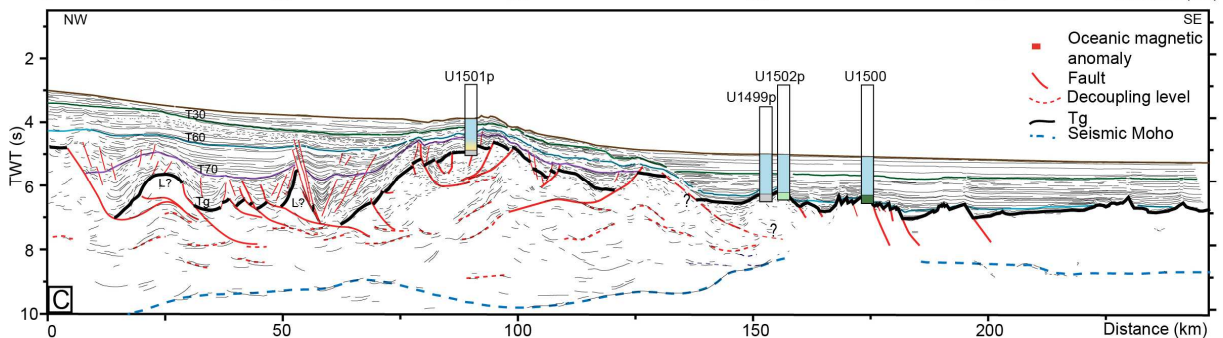
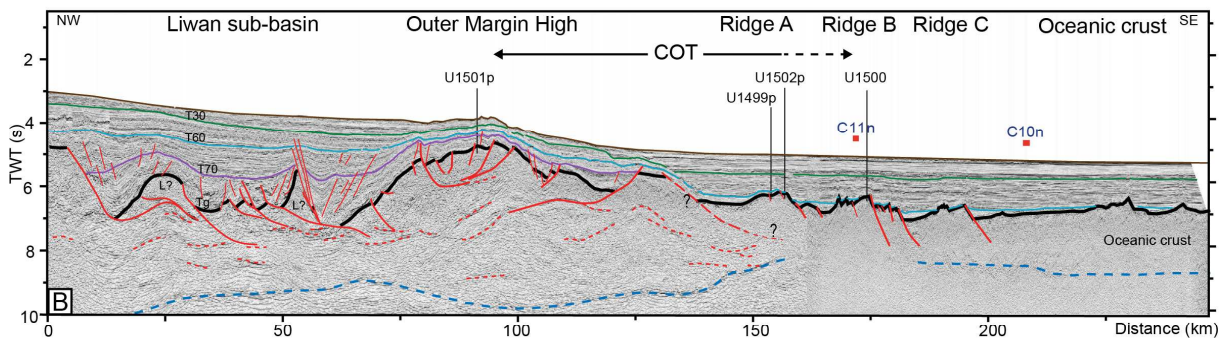
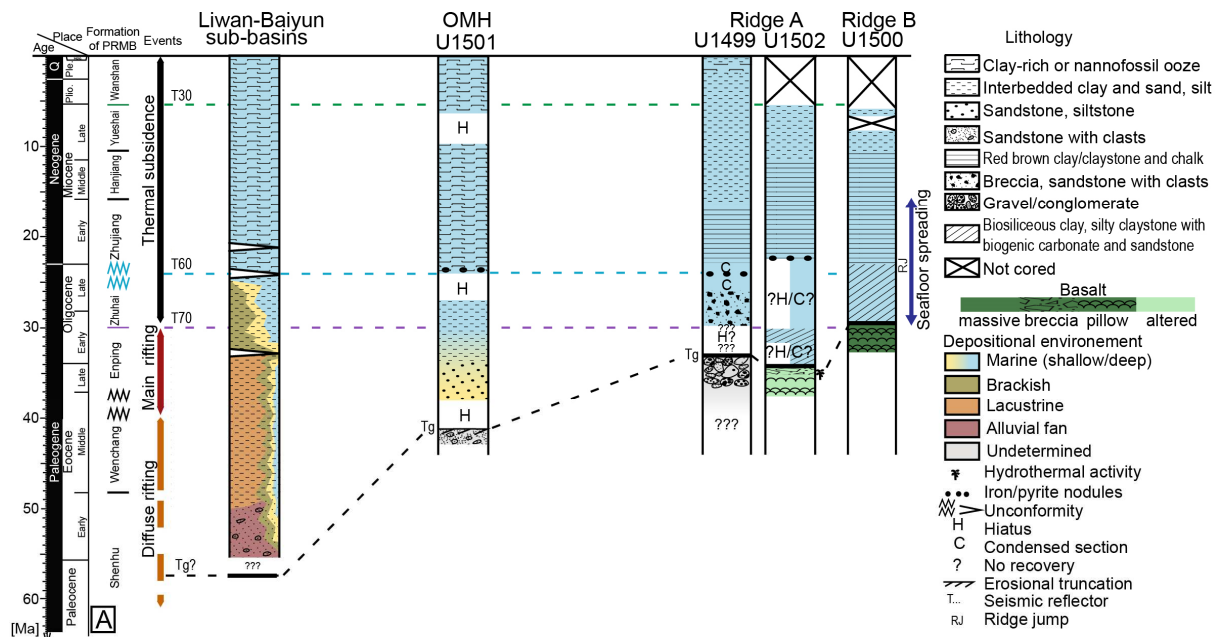
162
 163 **Figure 2: A) Crustal thickness map of the SE China margin determined by 3D gravity inversion B)**
 164 **Zoomed map of the Tg reflector (i.e. top acoustic basement, see text) on the margin segment cored**
 165 **during IODP Expeditions 367 & 368 (Larsen et al., 2019d), C) Rift domain map of the SE China**
 166 **margin. Picking of the oceanic magnetic anomalies from Biais et al., 1993**

167
 168 The later middle Eocene to early Oligocene rift event was associated in the PRMB with the
 169 deposition of the Wenchang lacustrine and the Enping lacustrine to shallow marine
 170 formations (Sizhong and Cunmin, 1993) (Fig. 3). These sedimentary sequences are
 171 contemporaneous with the formation of deep sedimentary basins (e.g. Baiyun, Liwan sub-

172 basins, Fig. 2) bounded by low angle extensional faults soling out at mid crustal levels (Savva
173 et al., 2014; Lei et al., 2019). This second event is interpreted to represent the main rifting
174 phase that thinned the continental crust (beta factor > 3) (Haizhang et al., 2017; Larsen et al.,
175 2018d)

176 Recent IODP scientific boreholes on the hitherto un-sampled distal margin recovered pre-
177 syn- and post-rift sediments (Fig. 3) (Larsen et al., 2018d). The sedimentary facies and
178 horizon ages of seismic interpretations, now firmly constrain continental breakup in the
179 Eastern SCS sub-basin to be in the Early Oligocene (~30 Ma) (Larsen et al., 2018d). However,
180 southwest of the PRMB, the continental extension continues into the lower Miocene and the
181 opening of the southwestern segment of the SCS.

182 Several authors (Holloway, 1981; Li and Li, 2007; Pubellier and Meresse, 2013; Taylor and
183 Hayes, 1983; Ye et al., 2018) proposed that during the Mesozoic, the northern margin of the
184 SCS was an “Andean” type active margin with compressional structures and important arc
185 magmatism related to the northward subduction of the proto-Pacific Ocean below the SE
186 China block. The last occurrence of subduction related magmatism is dated at 86 Ma (J. Li et
187 al., 2014), implying that no more than 50 Myrs separated convergence from initiation of SCS
188 rifting. This is less than the estimated time required for lithosphere to regain thermal
189 equilibrium (McKenzie, 1978).



190

191 **Figure 3: A) Summary charts of drilling results from IODP 367-368 (Larsen et al., 2018e). Synthetic**
 192 **stratigraphic columns of Liwan/Baiyun sub-basins (Morley, 2016). B) Seismic section 1555**
 193 **interpreted with the major horizons and unconformities (modified from Larsen et al., 2018d).**
 194 **Location of seismic section 1555 is presented in Figure 2. L indicates potential emplacement of**
 195 **laccolith; Tg, top of acoustic basement. C) Line Drawing of the seismic section 1555**

196

197 **2.2) The conjugate SE China-NW Palawan distal margins structure**

198 Plate kinematic reconstructions of Taylor and Hayes (1983) and Zahirovic et al., (2014)
199 identify the NW Palawan margin as the conjugate margin segment of the IODP studied
200 segment of the SE China margin within the western part of the Eastern sub-basin (Fig. 1). We
201 have selected representative seismic sections from each side of these two conjugate margins
202 segments to compare their development.

203 **2.2.1) The SE China distal margin**

204 The SE China margin facing the Eastern SCS oceanic sub-basin is a wide margin (> 400 km)
205 (Fig. 2). The PRMB occupies most of this margin with numerous deep rift basins (e.g. Baiyun,
206 Enping, Liwan sub-basins Fig. 2) separated by basement highs (e.g. Outer Marginal High,
207 Fig.2) which have been extensively investigated by seismic reflection data and industry
208 drilling (Gao et al., 2015; Lei et al., 2019; Lei and Ren, 2016; Zhou et al., 2018; Lei et al.,
209 2018). The PRMB developed during the Eocene to early Oligocene main rifting phase and
210 was later progressively filled by thick post-rift sedimentary sequences. Parts of the deeper
211 structures of the PRMB were likely inherited from the Mesozoic convergent setting as
212 expressed by remnants of thrust and folds in the substratum (Li et al., 2008; Ye et al., 2018).
213 Hydrocarbon exploration focuses on the proximal part of the margin (Ge et al., 2017), but
214 the more distal domain hosting the COT is nevertheless covered by high quality seismic
215 reflection (Ding et al., 2018; Gao et al., 2015), seismic refraction profiles (Lester et al., 2014;
216 Pin et al., 2001; Zhao et al., 2010) and potential field surveys (C.-F. Li et al., 2014). These data
217 constrained breakup models highlighting the lateral propagation of oceanic accretion
218 (Cameselle et al., 2017; Lei and Ren, 2016). In this study, we focus on a ~100km long
219 segment of the distal SE China margin (Fig. 2) where synchronous breakup and similar
220 deformation processes can be assumed. This margin segment is covered by high quality
221 seismic data (Fig. 4-5) and located at the western edge of the Eastern oceanic sub-basin
222 where seven deep scientific drill holes, including six reaching the acoustic basement have
223 been cored during IODP Expeditions 367-368 and 368X (Larsen et al., 2018d, Childress et al.,
224 2019) (Fig. 2). This segment is characterized by a major basement high referred to as the
225 Outer Marginal High (OMH) separating to the northeast the Liwan sub-basin, and to the
226 southwest the COT (Fig.3). Since the Oligocene breakup, no major tectonic event occurred
227 within this margin segment, while the subduction zone is located 500 km east of the
228 investigated margin segment.

229 **2.2.2) The NW Palawan distal margin**

230 The structure and rifting history of the NW Palawan margin are not constrained with dense
231 modern geophysical surveys and deep scientific boreholes, unlike the SE China margin.
232 However, available seismic profiles and industry wells (mostly from the proximal margin)
233 provide general constraints on the sedimentary evolution and margin architecture (Franke et
234 al., 2011; Schlüter et al., 1996; Steuer et al., 2013; Williams, 1997). A first order observation
235 is that the NW Palawan margin is much narrower (~180 km wide, Fig. 6) compared to the SE
236 China conjugate margin.

237 North Palawan is interpreted as formerly belonging to the South China block during the
238 Mesozoic and early Cenozoic and shows a similar tectono-stratigraphic evolution to the
239 Asian mainland (Fontaine, 1979; Holloway, 1981). The syn-rift sedimentary sequence of late
240 Eocene to Oligocene age is composed of fluvial to middle neritic interbedded siltstones and
241 sandstones in the proximal domains. In the distal domains, a few drill holes contain
242 continental to outer neritic facies and locally carbonate platforms on basement highs
243 (Franke et al., 2011; Schlüter et al., 1996; Williams, 1997). During rifting in the Eocene to
244 early Oligocene period, the NW Palawan block was also affected by the obduction of the
245 ophiolitic belt outcropping onshore (Faure et al., 1989). A tectonic quiescence followed this
246 synchronous extensional/compressional event with emplacement of the Nido carbonates, at
247 least on the proximal margin, that constitute the latest Eocene to early Miocene late syn- to
248 post-rift sediments (Fig. 7)(Fournier et al., 2005). Since the middle Miocene, the NW Palawan
249 block was affected by the ongoing collision between continental fragments (NW Palawan,
250 the Calamian Group, Mindoro), the magmatic arc and ophiolite units of Luzon in the east
251 (Karig, 1983), but none of this deformation affected the studied distal margin.

252

253 **3. Data and method**

254 **3.1) Dataset and mapping methodology**

255 The SE China margin is covered by a dense grid of geophysical data from which we use two
256 previously published reflection seismic profiles (lines 1555 and 1530 Figs. 4-5, acquisition
257 parameters can be found in Gao et al., 2015). These profiles are located near to IODP drilling
258 Sites (Figs. 2, 3, 4 and 5). For the NW Palawan margin, we use the reflection seismic profile
259 (BGR08-109 Fig. 6, 7) published by Franke et al. (2011). In addition, we include in our analysis

260 of the area: 1) a range of published seismic dataset acquired by both academic and industrial
261 surveys (Cameselle et al., 2017; Lei et al., 2019; Yang et al., 2018); 2) a compilation of
262 structural maps (Cullen et al., 2010; Pubellier et al., 2017); 3) different borehole data (Larsen
263 et al., 2018e; Li et al., 2015; Wang et al., 2000); 4) magnetic and gravity grids (Doo et al.,
264 2015; Meyer et al., 2017; Sandwell et al., 2014); 5) refraction lines (Ding et al., 2012; Pichot
265 et al., 2014; Pin et al., 2001); and 6) crustal thickness mapping determined by gravity
266 inversion (Gozzard et al., 2019).

267 We follow the rift domain mapping methodology applied for hyper-extended magma-poor
268 margins located around the southern North Atlantic (Nirrengarten et al., 2018; Peron-
269 Pinvidic et al., 2013) on the SE China-NW Palawan conjugate margins (Fig. 2,6). This method
270 is based on the identification of characteristic elements of each rift domains such as crustal
271 thickness, structural style, accommodation space and geometry of the sedimentary infill (for
272 a detailed description see Tugend et al., 2015). Several domains were defined alongside both
273 margins such as: proximal, thinned and hyper-thinned domains, distal highs, COT, oceanic
274 crust (Fig. 2-6). In this study, the proximal domain is defined by a crustal thickness exceeding
275 30 km on the gravity inversion crustal thickness map (Fig.2). In seismic sections this domain
276 is characterized by small rift basins bounded by high angle normal faults. The thinned and
277 hyper-thinned domains correspond to continental crust moderately (~30 -15 km thick) to
278 highly thinned (<15 km thick), respectively. Distal highs are present along the SCS margins
279 and correspond to positive basement topography with some of them showing a bathymetric
280 expression today. These distal highs generally delimit thinned or hyper-thinned domains
281 from those of the COT. The COT is located from the distal high to the first igneous oceanic
282 crust. It is composed of the most distal hyper-thinned continental crust overprinted by
283 magmatic additions (Larsen et al., 2018d). The oceanic crust is defined by fully new igneous
284 crust with a crustal thickness ranging from 5 to 7 km (~2s Two Way Travel Time: TWT).
285 Hence the COB (Continent-Ocean Boundary) is the continentward limit of the oceanic crust.

286 **3.2) Quantitative analysis methodology: 3D gravity anomaly inversion and joint** 287 **inversion of seismic reflection and gravity data**

288 In order to determine Moho depth and crustal basement thickness on the SCS rifted margins
289 we perform 3D spectral domain gravity inversion following the scheme of Parker (1972)
290 together with a correction for the lithosphere thermal gravity anomaly and a
291 parameterization of decompression melting to predict magmatic addition (Chappell and

292 Kuzsnir, 2008, Alvey et al. 2008, Kuzsnir et al. 2018). Only public domain data are used for
293 the 3D mapping procedure: free-air gravity anomaly data (1 arc-minute resolution; Sandwell
294 et al., 2014; see supplementary material 1), bathymetry ETOPO1 (1 arc-minute resolution;
295 Amante and Eakins, 2009), NOAA sediment thickness (5 arc-minutes resolution; Whittaker et
296 al., 2013) and oceanic crust age (6 arc-minute resolution; Müller et al., 2016). Prior to the 3D
297 spectral inversion to determine Moho depth, a Butterworth low-cut filter with cut-off
298 wavelength 100 km is applied to the Moho residual gravity anomaly to remove short
299 wavelengths. This gravity inversion scheme invokes Smith's theorem (Smith, 1961) which for
300 the assumptions made provides a unique solution for 3D Moho depth and crustal basement
301 thickness (Chappell & Kuzsnir 2008)

302

303 We follow the parameterization of Gozzard et al., (2019), who performed extensive
304 sensitivity tests on the free-air gravity anomaly inversion for the SCS to determine crustal
305 basement thickness and continental lithosphere thinning. Our preferred solution uses a
306 reference Moho depth at 40 km, normal volcanic addition (giving a 7 km thick oceanic crust)
307 and a breakup age at 33 Ma corresponding to the oldest oceanic crust in the SCS. Gravity
308 inversion using these parameters predicts the seismically observed thicknesses of oceanic
309 crust in the study area. The sensitivity tests carried out by Gozzard et al., 2019 demonstrated
310 the critical importance of including the lithosphere thermal gravity anomaly correction in the
311 gravity inversion.

312

313 The 3D gravity anomaly inversion map is improved by the integration of more precise
314 sediment thickness data of seismic lines 1555, 1530 and BGR08-109 (Fig. 4, 5 &7) (Franke et
315 al., 2011; Gao et al., 2015; see supplementary material 2). Sediment thickness is based on a
316 time to depth conversion using depth-time functions established at Sites U1500 and U1499
317 for the COT and oceanic domain of lines 1555 and 1530 (Stock et al., 2018; Sun et al., 2018).
318 However application of this depth conversion produces unrealistically large interval seismic
319 velocities for sediments in the deeper parts of the Liwan sub-basin as T_g is approached. As a
320 consequence for the Liwan sub-basin (NW of the OMH) and the Palawan section, in the
321 absence of seismic velocity–depth measurements from well data, we use a seismic velocity-
322 depth relationship of $V_p = V_o + k.z$ for depth conversion where $V_o = 1.75 \text{ km.s}^{-1}$, $k = 0.4 \text{ km.s}^{-1}.$
323 km^{-1} and z is in km. This avoids very large and unrealistic interval velocities in the deepest

324 parts of the Liwan sub-basin. It should be noted that this uncertainty in the Liwan sub-basin
325 does not adversely affect our gravity inversion analysis in the COT.

326 To determine the lateral variation of crustal basement density across the COT margin we
327 perform a joint inversion of the deep seismic reflection interpretation and gravity anomaly
328 data for lines 1555, 1530 and BGR08-109 (Fig. 4, 5 & 7) following the method described in
329 Cowie et al. (2017) and Harkin et al. (2019). This method compares Moho depth determined
330 from gravity inversion with the interpreted seismic Moho TWT in the time domain. By
331 matching the gravity Moho taken into the time domain with the Moho TWT from seismic
332 interpretation, the lateral variation in vertically averaged basement density and seismic
333 velocity can be determined. The conversion of Moho depth to TWT in the time domain
334 requires a value for basement seismic velocity which we determine using an equation linking
335 basement seismic velocity with basement density. In this study we use a linear empirical
336 relationship ($V_p = 2.27.\rho + 0.25$) linking seismic velocity (V_p , in km/s) and density (ρ , in gm/cc)
337 for crustal basement determined from the velocity-density compilation presented by Birch
338 (1961) for crystalline crustal basement rocks. An alternative velocity-density relationship
339 based on the Nafe-Drake relationship (Ludwig et al., 1970; Brocher, 2005) has also been
340 examined, however the relationship derived from Birch (1961) gives a more stable joint-
341 inversion and is also more appropriate for crystalline crustal basement. In the initial gravity
342 inversion (prior to the joint inversion iterations), a uniform basement density of 2.85 g.cm^{-3}
343 used.

344 The lateral variation of basement density affects the depth of the Moho predicted from
345 gravity inversion, while the lateral variation of basement seismic velocity affects the
346 conversion of the gravity inversion Moho from the depth to the time domain. The joint
347 inversion requires an iterative adjustment of both basement density and seismic velocity,
348 which are linked by the velocity-density relationship described above, until convergence is
349 achieved. The advantage of comparing the gravity Moho depth with the seismic Moho in the
350 time domain rather than the depth domain is that this approach avoids the uncertainties in
351 basement seismic velocity which are used in making the seismic reflection depth section. It
352 also provides a powerful technique for validating Moho seismic interpretations.

353 The method assumes that the sediment thickness (depth to top basement), used in the
354 gravity inversion and derived from the seismic reflection interpretation and depth

355 conversion, is correct. The gravity inversion Moho depth (and seismically determined depth
356 to top basement) is used to determine crustal basement thickness which is converted into
357 the time domain (as an interval TWT). This interval TWT is then added to the seismic
358 interpretation of top basement in TWT to determine the conversion of the gravity inversion
359 Moho in depth into the time domain for direct comparison with the seismic Moho TWT.

360 The lateral density variations of crustal basement along a transect are used to identify lateral
361 variation in the nature of the crust. This joint inversion is pertinent only when the Moho
362 reflector is well imaged on the seismic sections. The joint inversion analysis was performed
363 across the entire SE China margin and adjacent oceanic crust for seismic lines 1555 and
364 1530, but only on the oceanic and COT domains of the NW Palawan margin for seismic line
365 BGR08-109 (Fig. 4, 5 &7)

366

367 **4. Architecture of the SE China margin**

368 **4.1) Mapping of the rift domains**

369 Our map of rift domains of the SE China margin shows an alternation of deep rift basins
370 separated by basement highs (Fig. 2). The Zhu I-III and Enping sub-basins are aligned and
371 elongated along a NE-SW axis (Fig. 2). These basins are characterized by moderate crustal
372 thinning (~20 km thick) and constitute the “thinned domain” (Fig. 2A-C). Further seaward,
373 the Baiyun and Liwan sub-basins occupy a central position in the margin representing the
374 “hyper-thinned domain”. Several studies (Lei et al., 2019; Wang et al., 2018; Zhou et al.,
375 2018) show that these basins are floored by hyper-thinned crust (<15 km thick) in relation
376 with low angle extensional faults rooting at mid-crustal level. The Baiyun sub-basin is
377 separated from the Enping sub-basin to the NW and the Liwan sub-basin to the SE by two
378 basement highs with thicker continental crust (~20km). The Liwan sub-basin is separated
379 from the COT by the OMH. This distal high (OMH) shows a significantly shallower Tg (base
380 Cenozoic, see below) on the basement reflector TWT depth map (Fig. 2B). The COT bounding
381 the oceanic domain is 50 to 80 km wide. The mapped COB is segmented by fracture zones. In
382 our focus area (Fig. 2B) a sharp transfer zone is observed to the SW and a more diffuse
383 system to the NE delimiting a ~150km wide margin segment.

384 **4.2) Seismic architecture and correlation with IODP data**

385
386 The deep seismic profiles 1555 and 1530 image the distal part of the SE China margin close
387 to the location of the IODP Sites from Expeditions 349, 367, 368 and 368X (Figs. 3-5). Across
388 these two profiles a strong reflector (Tg) can be consistently identified. Tg is the top of
389 acoustic basement, which corresponds locally to the base of the Cenozoic sequence (Fig. 3).
390 The mapping in TWT of Tg reflector across the studied segment of the distal SE China Sea
391 margin (Larsen et al., 2018e) highlights the 3D architecture of this area (Fig. 2B). From
392 northwest to southeast, the following distinct structural features have been recognized (Figs.
393 3, 4-5): 1) The Liwan sub-basin; 2) The OMH; 3) The COT; 4) Ridges A, B, C; and 5) The
394 oceanic crust (Larsen et al., 2018e). Besides the Tg reflector, key seismic horizons have been
395 determined by correlation between stratigraphic well data and interpreted seismic sections
396 (e.g. Larsen et al., 2018d; Lei et al., 2019). The following seismic horizons used in this study
397 are: T70 corresponding to the top of syn-rift sequence, T60 representing a regional
398 unconformity around Oligocene-Miocene boundary (28-24 Ma) and T30 correlating with the
399 top of the Miocene (Fig. 3).

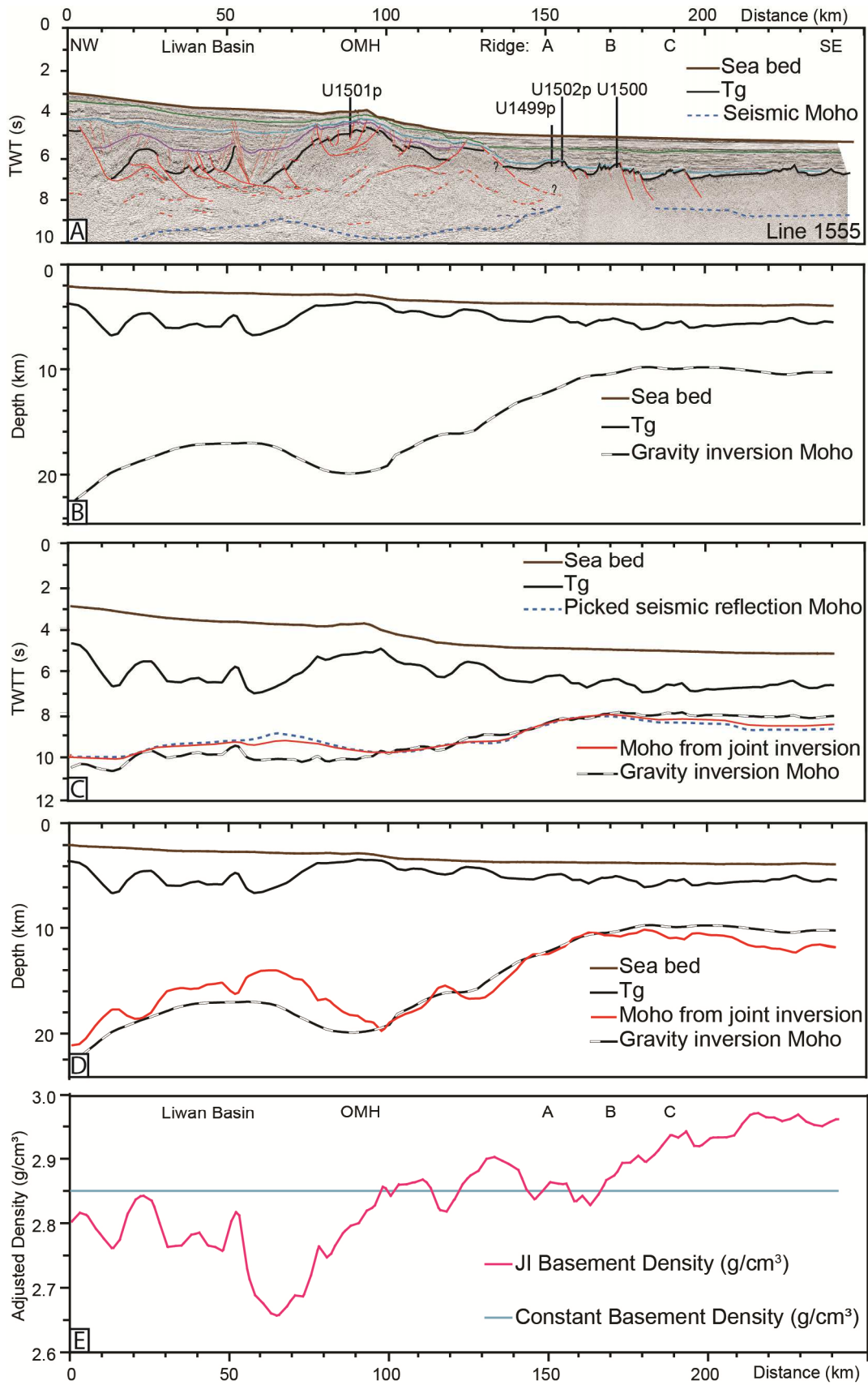
400 Seismic lines 1555 and 1530 have been previously described in several previous
401 contributions (Gao et al., 2015, Larsen et al., 2018d). In this section, these works are
402 summarized together with new observations that led to propose new interpretations
403 especially for the COT structure. Seismic line 1555 crosses central part of the Liwan sub-
404 basin whereas seismic line 1530 captures only its southwestern edge. The Liwan sub-basin
405 shows a thick Cenozoic post- to syn-rift succession reaching a thickness of 3.5 s TWT in its
406 central part. The large-scale basin architecture is characterized by a large-scale low angle
407 extensional fault on the northwestern boundary of the basin (at 10 km Fig. 3-4). Seismic line
408 1555 shows contrasting sedimentary package morphologies at the base of the syn-rift
409 sequence (Tg-T70 interval Fig. 3) delimiting several sub-basins bounded by oceanward
410 dipping low angle extensional faults, which soles out on different decoupling levels (Lei et al.
411 2019, Zhang et al., 2019). A strong amplitude reflector is well imaged at about 9 s TWT
412 inboard and is interpreted as the Moho reflection. The continental basement is extremely
413 thinned in the Liwan sub-basin (2.5 s TWT from Tg to the Moho) locally reaching only 8 km of
414 thickness in some area (Wang et al., 2018). Notably, the early Cenozoic Wenchang formation
415 (early/mid Eocene ~56-40 Ma) known from the more proximal basins is not clearly

416 recognized in the deep Liwan sub-basin (Haizhang et al., 2017). In contrast, the main rifting
417 phase of this basin is interpreted as middle Eocene to early Oligocene (Larsen et al., 2018d)
418 suggesting that the Liwan sub-basin resulted mostly from the main, second rifting event
419 affecting the PRMB. The syn-rift sedimentary package presents locally small flexures (<10 km
420 wide, at 50-75 km Fig. 3) interpreted by Clift et al., (2015) to result from increased lower
421 crustal flow induced by sediment loading. Alternatively, (Zhang et al., 2019) suggested that
422 magmatic intrusions with possible laccolith geometries (at 20 km and 50 km Figs. 3-4) might
423 be present and responsible for these small flexures.

424 Despite some significant morphological variations of the OMH in our two seismic profiles, it
425 generally corresponds to a basement high, with T_g being 2-3s TWT shallower than within the
426 Liwan sub-basin. The major intra-crustal reflections observed below the Liwan sub-basin can
427 be followed until the southeastern tip of the OMH at the depth of 7 to 8 s TWT. Interestingly,
428 the Moho below the OMH is interpreted at 9.5-10 TWT, thus 0.5-1s deeper than below the
429 Liwan sub-basin. The OMH shows significant along strike structural variation: In line 1555
430 (Fig 4.), the OMH shows a general dome shape while in line 1530 it consists of two basement
431 ridges reaching the seafloor (Fig. 5, at 25 km & 50 km). These basement ridges form
432 continuous structures on a WNW-ESE trend over 10 to 20 km observed on free-air gravity
433 maps (Supplementary material 1). These highs are inferred to be continental basement
434 possibly associated with local syn- or post-rift magmatic additions (Gao et al., 2015; Wang et
435 al., 2006; Zhang et al., 2019).

436 On the OMH, at Site U1501 a hiatus of ~4Ma (24-28 Ma, Jian et al., 2019 Fig. 3) is observed
437 and marked by the T₆₀ reflector which corresponds to an unconformity dated at 24Ma. At
438 Site U1505, T₆₀ is not a sedimentary hiatus (Jian et al., 2018), but both drill sites show a
439 distinct change in sediment facies from post-rift carbonate rich marine sediment above T₆₀
440 to a fining upward clastic sedimentary sequence below T₆₀ (Larsen et al., 2018c) (Fig. 3).
441 The syn-rift package (T₇₀-T_g interval) is offset by several high-angle normal faults verging
442 either ocean- or continent-ward forming small syn-rift basins filled by clastic sedimentary
443 sequences (Larsen et al., 2018a). The oldest age of this syn-rift sequence was obtained ~200
444 m above its base (T_g) and is dated at ~34 Ma (Larsen et al., 2018a). The syn-rift clastic
445 sedimentary facies within Site U1501 are similar to the Eocene Enping formation composed
446 of deltaic to shallow marine sandstone reported in the more proximal basins of the PRMB
447 (Xia et al., 2018)(Fig. 3). Below the T_g reflector, well lithified pre-rift conglomeratic

448 sandstones of unknown age were recovered at Site U1501 (Fig. 3). Close to Site U1501, Tg
449 truncates low-amplitude sub-Tg reflectors, along with a strong contrast in the degree of
450 lithification this support significant erosion prior to the deposition of the syn-rift sequence,
451 and hence, the presence of a major hiatus (Larsen et al., 2018a).



452

453 **Figure 4: A) Seismic profile 1555 crossing the SE China COT modified from Larsen et al., 2018d**

454 **(location of Line 1555 in Fig. 2). B) Depth converted Tg and Moho determined by 3D gravity**

455 **anomaly inversion. C) Time cross section comparing the Moho predicted from gravity anomaly**
456 **inversion converted into time, the picked seismic Moho and the joint inversion Moho. D)**
457 **Comparison in depth between the Moho determined by joint inversion and the Moho determined**
458 **by gravity anomaly inversion. E) Lateral variations in basement density along the line 1555. The**
459 **blue line corresponds to a density of 2.85 g/cm³, which is the reference basement density used**
460 **within the gravity anomaly inversion.**

461

462 From the OMH to Ridge A the continental crust thins with the Moho rising from ~9 to ~7.5 s
463 TWT. Continentward low angle extensional faults are observed in this area, but a major
464 oceanward structure is interpreted at 135 km, offsetting Tg (Fig. 3). Ridge A is a ~10 km wide
465 basement high, bounded by an oceanward dipping low angle extensional fault to the
466 southeast. The Tg reflector at Ridge A shows low amplitude and variable continuity below
467 which some reflectors indicate the presence of layered lithologies, possibly including
468 sedimentary deposits. Ridge A (Figs. 2.b, 3) has been drilled at Site U1499 (Sun et al., 2018)
469 on line 1530 and at Site U1502 (Larsen et al., 2018b) located 10 km to the east of line 1555.
470 Site U1499 sampled post-rift, monotonous turbiditic sediments followed by a succession of
471 lowermost Miocene and upper Oligocene fine-grained red clay, with strongly lithified pelagic
472 red claystone (Sun et al., 2018). Below the red clay, the cored intervals recovered coarse
473 siliciclastic sediments composed from top to bottom by a matrix supported breccia with
474 angular and pebble-sized clasts, and a succession of very coarse-grained gravel, mostly
475 consisting of cobble-sized clasts. All clasts represent previously eroded sedimentary rocks
476 (mostly coarse-grained sandstone with some lithic fragments) (Fig. 3). The matrix supported
477 breccia is deposited in a deep marine environment between 26 and 30 Ma and represents
478 the earliest post-rift sedimentary unit. The origin of the lowermost gravel unit (pre 30 Ma)
479 remains largely non-constrained as no depositional environment or age has been
480 determined (Fig.3). It could be of early syn-rift age, but also of pre-rift age, but in any case a
481 tectono-sedimentary shift occurred between these two units (Sun et al., 2018). Ridge A was
482 also sampled 40 km to the East at Site U1502 and shows a post-rift succession similar to that
483 of Site U1499. Below the post-rift succession, recrystallized dolomite related to
484 hydrothermal processes alternates with claystone containing agglutinated benthic
485 foraminifers suggesting an age as old as the late Eocene (Larsen et al., 2018d). The basement
486 is made of highly altered MORB that suffered pervasive hydrothermal activity that in part

487 extended into the lowermost overlying sediments (Larsen et al., 2018d), and hence,
488 constrained basalt age to be more or less the age of the lowermost, hydrothermally altered
489 sediments.

490 Ridge B (Fig. 2.b) is located 13 km southeastward of Ridge A and is a ~15km wide basement
491 high. Its morphology is controlled by two main high-angle normal faults dipping oceanward,
492 rotating top basement landwards, and displacing top basement by as much as 0.2s TWT (Fig.
493 3). Site U1500, located on Ridge B, cored deep marine pelagic sediments of Miocene to
494 Oligocene age. These sediments overlie fresh MORB presenting pillow structures and
495 intercalated sediments containing calcareous nannofossils indicating an Oligocene age (Stock
496 et al., 2018). The marine magnetic anomaly C11n (30 Ma; Gee and Kent, 2007) mapped by
497 (Briais et al., 1993) is closely aligned with Ridge B (Fig. 2). Based on clear sub-Tg seismic
498 layering along a strike line through Site U1500, Larsen et al. (2018d) interpreted the volcanic
499 edifice of MORB to extend to at least 2 km below Tg. The Moho reflection is absent below
500 Ridge B along line 1555 (Fig. 3-8). However, in line 1530, a step in a better developed Moho
501 reflection is observed between ridges A and B at 130 km (Fig. 5) and could correspond to the
502 transition between “continental” and “oceanic” Moho. Locally on seismic sections, on top of
503 the basement a thin and tilted sedimentary layer is observed related either to fault activity
504 or to pelagic draping. This sedimentary layer was likely deposited during early Oligocene but
505 no later than late Oligocene (Stock et al., 2018). With the exception of one fault bounded
506 basin, no sedimentary fans are observed in relation with the faulting of Ridge B, suggesting a
507 short time lag between basalt formation and faulting.

508 The most distal Ridge C (Fig. 2b) is located ~15 km further SE of Ridge B. It is characterized by
509 rotated fault blocks bounded by oceanward dipping high-angle normal faults. Moho
510 reflection reappears at this position around 8 s TWT on line 1555. The igneous nature of
511 Ridge C has been confirmed by drilling at Site U1503 (Childress, 2019). As for Ridge B, the
512 seismic data strongly suggests that the faulting took place shortly after the emplacement of
513 the igneous rocks (Fig. 3).

514 The southeastern part of the two seismic sections (Fig. 4-5) presents a relatively smooth and
515 flat Tg reflector parallel to the Moho reflection. These two reflectors are separated by 2 s
516 TWT and show no major tectonic features as expected for oceanic crust. Marine magnetic
517 anomalies C10n (Briais et al., 1993) dated at 28.7 Ma (Gee and Kent, 2007) is located slightly

518 southeastward of Ridge C suggesting that MORB magmatism at this ridge has an age ranging
519 between 30 Ma and 28.7Ma.

520 **4.3) Gravity anomaly and joint inversions of gravity and seismic data**

521 *Line 1555*

522 The Moho depth along seismic line 1555 has been determined using 3D gravity anomaly
523 inversion using the interpreted depth converted sediment thickness from the seismic
524 profiles (from seabed to Tg) (Fig. 4B). The resulting depth section (Fig. 4B) confirmed
525 significant crustal thickness and architecture variations described previously from 1555 time
526 section along the SE China margin. In this profile, the main depocentre of the Liwan sub-
527 basin reaches up to 5 km of Cenozoic sediments overlying an 11 km thick continental
528 basement. The crustal thickness below the OMH is around 16 km and progressively thins
529 toward the COT and oceanic crust which show a thickness of 5 to 6 km (Fig. 4B). Notably, a
530 shift in the Moho geometry occurs between ridges A and B at ~165 km passing from a
531 gradual rise to a sub-horizontal geometry.

532 The Moho depth predicted from gravity inversion has been converted into the time domain
533 for comparison with the Moho TWT interpreted from the seismic reflection data. A
534 basement density of 2.85 g.cm^{-3} is initially used in the gravity inversion (Chappell and
535 Kuszniir, 2008) (Fig. 4C). The crustal basement thickness from gravity inversion is converted
536 into the time domain to give an interval TWT using a basement seismic velocity calculated
537 using the velocity-density relationship ($V_p = 2.27 \rho + 0.25$) described in section 3.2. This
538 interval TWT is then added to the seismic interpretation of top basement in TWT to give the
539 conversion of the gravity inversion Moho in depth into the time domain for direct
540 comparison with the seismic Moho (TWT). As discussed earlier this allows the time
541 converted gravity inversion Moho to be compared with the picked seismic Moho (Fig. 4C).
542 The gravity inversion Moho below the Liwan sub-basin is on average 0.5s deeper than the
543 picked seismic reflection Moho. From 110 to 180 km the seismic and gravity Mohos match
544 well and from 180 km to the end of the line the gravity Moho is on average 0.3 s shallower
545 than the seismic Moho. Joint inversion of the seismic and gravity data has been used to
546 determine the combination of basement seismic velocities and densities required to match
547 the Moho from gravity anomaly inversion with the picked Moho in the time domain. This
548 matching of seismic and gravity Mohos results in a joint inversion Moho along profile 1555

549 (Figs. 4C, D). Figure 4E shows the lateral variation of the vertically averaged basement
550 density resulting from the joint inversion. In comparison to the initial uniform basement
551 density of 2.85 g.cm^{-3} , a deficit of mass below the Liwan sub-basin and an excess of mass
552 oceanward of Ridge B are predicted by the joint inversion. Within the Liwan sub-basin the
553 maximum deficit is 0.17 g.cm^{-3} in the deepest part of the basin corresponding to a crustal
554 basement density of approximately 2.73 g.cm^{-3} . This average deficit could be related to the
555 crustal composition and to heterogeneities within basement. We suggest that in this case,
556 the deficit of mass located below Tg in the Liwan sub-basin may be related to pre-Cenozoic
557 sediments or stacked meta-sediments of the Yenshanian orogeny which effectively reduce
558 the average density of the crust. Interestingly, any syn-rift magmatism, if at all present, is
559 likely to be rather limited as it would push the average density upwards. On the OMH,
560 crustal densities vary but are in average higher than the densities on the Liwan sub-basin
561 and closer to the reference basement density of 2.85 g.cm^{-3} .

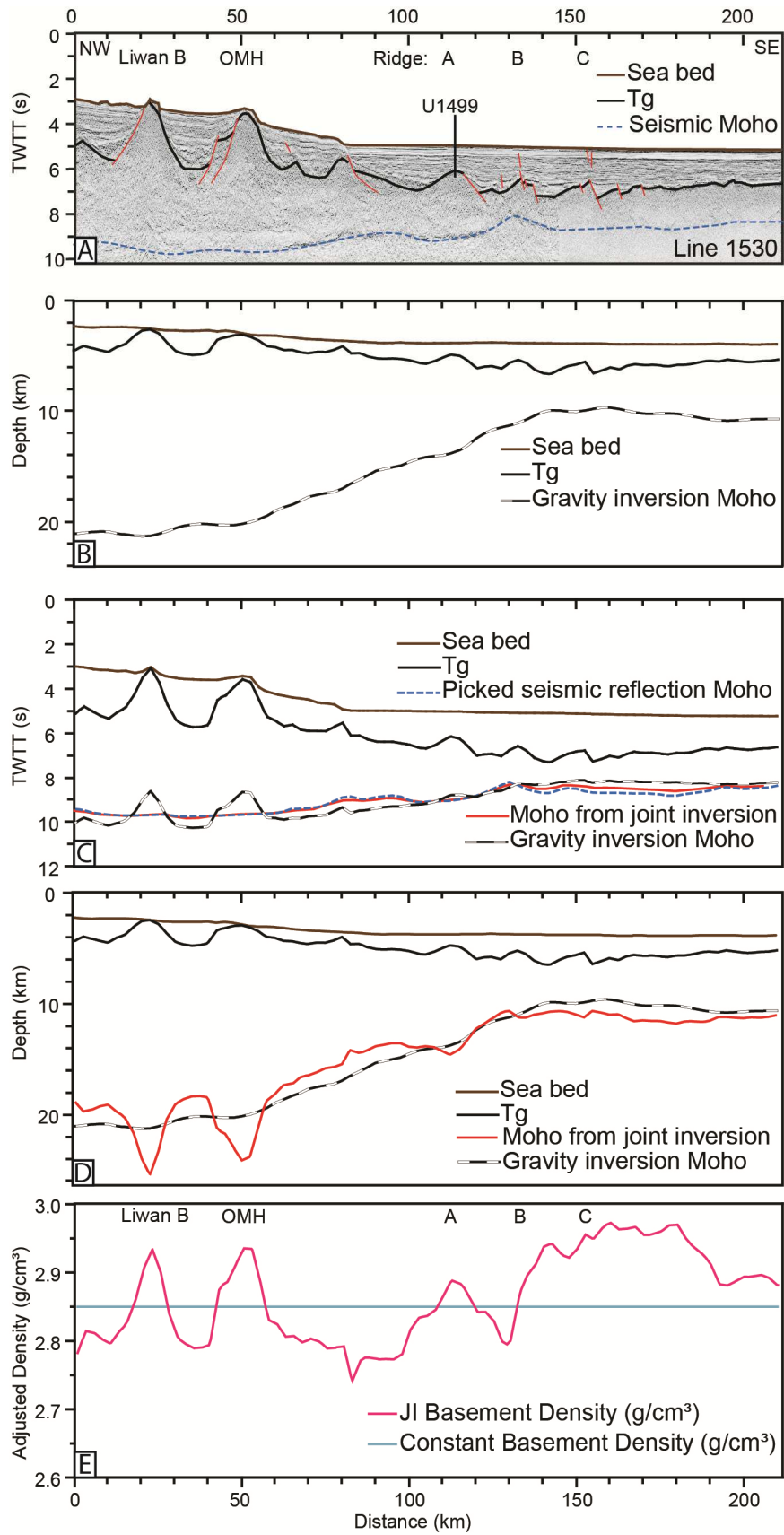
562 A major increase of estimated joint inversion densities occurs from 160 to 180 km on the
563 profile 1555 (from ridges A to B), corresponding in depth section to a step of the Moho
564 geometry (Fig. 4). Oceanward of this area, the average basement density rises to 2.93 g.cm^{-3} ,
565 which is close to the mean oceanic crust density of 2.89 g.cm^{-3} (Carlson and Raskin, 1984).
566 Therefore, we located the COB near 163 km where the density passes over 2.85 g.cm^{-3} ,
567 which likely corresponds to the formation of a new igneous crust.

568 *Line 1530*

569 We have applied the same procedure to line 1530 as for line 1555 (Fig. 5). The gravity
570 inversion Moho is almost flat from 0 to 50 km at a depth of 21km (Fig. 5B). The influence of
571 the two basement highs on the gravity inversion Moho is minor and limited to a Moho 1km
572 deeper than under the adjacent basins. The Moho shallows progressively from ~ 20 km deep
573 at the edge of the OMH to 10 km depth below Ridge B. The crust is 2 km thicker below Ridge
574 A on this line than on line 1555. The entire oceanic domain is characterized by a constant
575 Moho depth around 10 km and the crustal thickness ranges from 5 to 6.5 km thickness.

576 Conversion of the gravity inversion Moho to seismic reflection time (Fig. 5C) shows a deeper
577 gravity Moho compared to the picked seismic Moho from 0 to 110 km except on the two
578 basement highs of the OMH and Ridge A. It is notable that the seismic Moho TWT under the
579 two basement highs is flat and shows no signs of velocity pull-up. From kilometre 110
580 onward the gravity inversion Moho is shallower than the picked seismic Moho. On the

581 density profile (Fig5. E), the average crustal density until kilometre 110 is below the density
582 used in the gravity anomaly procedure (2.85 g.cm^{-3}) except on the two basement high. This
583 may imply that the continental crust is not a standard two layered continental crust, but has
584 a composition that reduces the mean crustal density, which would be in agreement with a
585 heterogeneous arc crust with nappe stacked, sedimentary basins and magmatic intrusions
586 inherited from the Yenshanian orogeny. As a result, the Liwan sub-basin basement may
587 partly be composed of metasediments whereas the OMH may contain denser magmatic
588 intrusions. North-eastward along the margin, high density lower crustal bodies (Lester et al.,
589 2014) are inferred to exist and suggests heterogeneity of the crustal layers. As for the
590 section 1555, a major step in the density passing from below 2.85 to above 2.90 g.cm^{-3} is
591 located at the transition between ridges A and B and related to the COB.



592

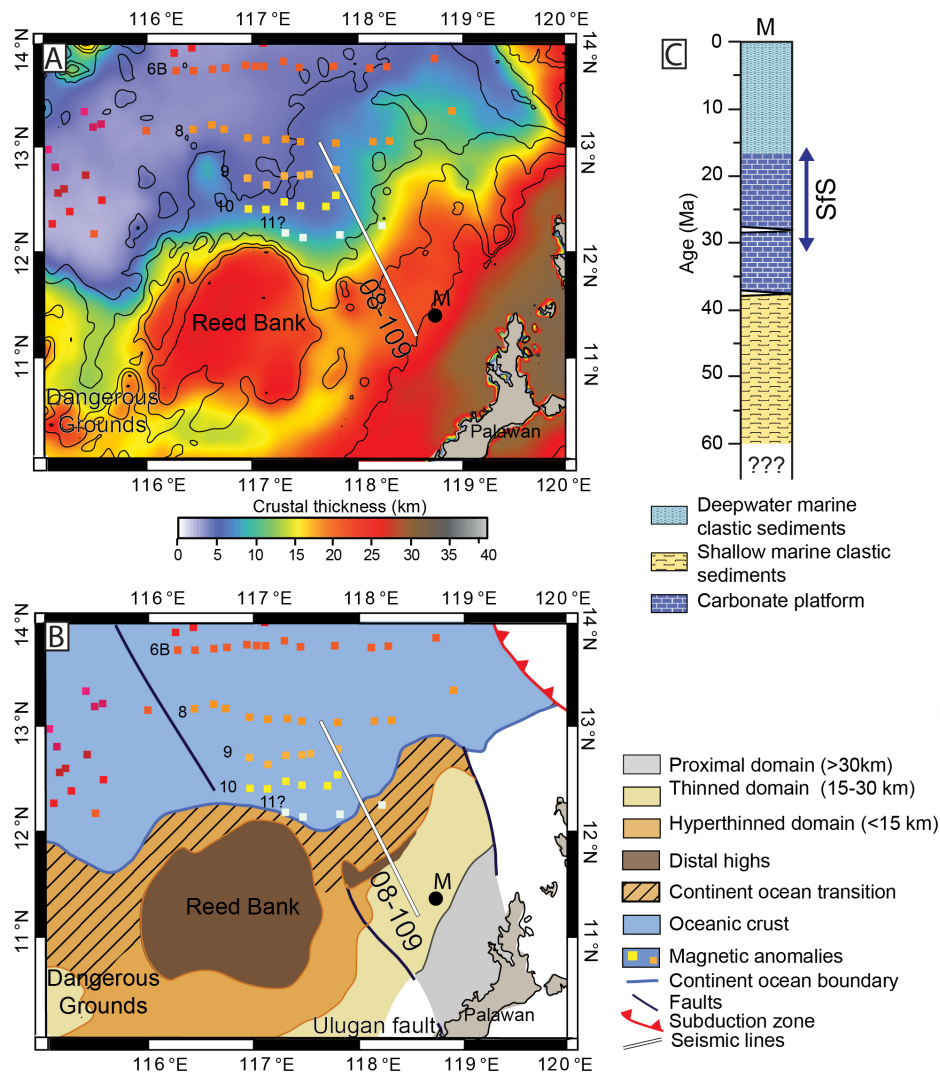
593 **Figure 5: A) Seismic profile 1530 crossing the SE China COT (modified from Gao et al., 2015; Line**
 594 **location in Fig.2). B) Depth converted Tg and Moho determined by 3D gravity anomaly inversion. C)**

595 Time cross section comparing the Moho predicted from gravity anomaly inversion converted into
596 time, the picked seismic Moho and the joint inversion Moho. D) Comparison in depth between the
597 Moho determined by joint inversion and the Moho determined by gravity anomaly inversion. E)
598 Lateral variations in basement density along the line 1530. The blue line corresponds to a density
599 of 2.85 g.cm^{-3} , which is the reference basement density used within the gravity anomaly inversion.

600 **5) Architecture of the NW Palawan margin**

601 **5.1) Mapping of the rift domains**

602 The NW Palawan margin is separated to the southwest from the Reed Bank by the Ulugan
603 fault zone, which forms the northern boundary of the Borneo-Palawan trough (Fig. 6). To the
604 northeast, the margin is bounded by a fault zone marking the western boundary of the
605 domain affected by the eastward dipping subduction zone. The crustal thickness map
606 (Fig.6A) highlights the differences in the thinning pattern of these three segments. The
607 Dangerous Grounds constitute a wide zone (>300km) where the continental crust in general
608 is thinned to less than 15 km with some narrow, SW-NE elongated ribbons of thicker crust
609 (see Pichot et al., 2014; Gozzard et al., 2019). At the opposite, the Reed Bank is a massive
610 basement high which thins rapidly toward the COT. On the NW Palawan margin, conjugate
611 to the studied SE China segment, the proximal domain trends parallel to the coastline (Fig.
612 6), and the thinned domain is often separated from the COT domain by narrow structural
613 highs as observed by Franke et al. (2011). The COT seems partly oblique to the marine
614 magnetic anomalies suggesting an initially complex evolution. This is further suggested by
615 the only sporadic and indirect indication of a possible presence of C11n (Fig. 6)(Briaies et al.,
616 1993), which is well defined on the SE China conjugate margin segment.



617

618 **Figure 6: A) Crustal thickness map of the NW Palawan margin determined by 3D gravity inversion**

619 **B) Map of the rift domains. Magnetic anomalies are from Briais et al., 1993. M: Malanpaya**

620 **borehole. C) Synthetic stratigraphic columns of Northwest Palawan margin (based on the**

621 **Malampaya borehole (Fournier et al., 2005). Sfs: seafloor spreading.**

622

623

624 **5.2) Seismic description of line BGR08-109**

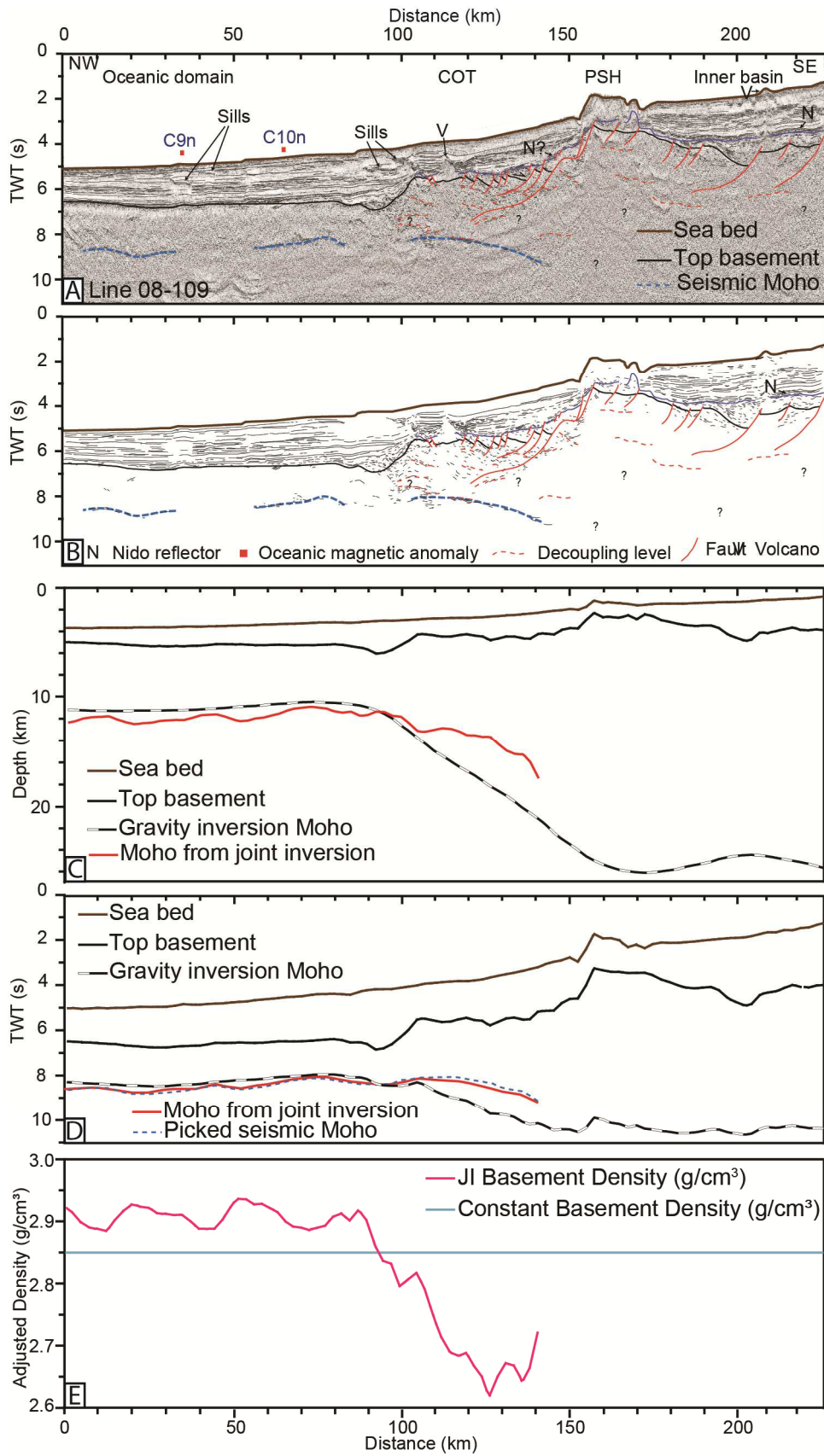
625 The seismic line BGR08-109 (Fig. 7) crosses the NW Palawan margin on a segment described
 626 previously by Franke et al. 2011. Several structural domains have been identified in this
 627 margin: a wide inner basin (>50 km wide), the narrow Palawan structural high (PSH), the COT
 628 and the oceanic crust.

629 The inner basin is defined by a basement that is offset by a series of normal faults controlling
630 thin wedge-shaped syn-rift sedimentary packages. This basin is thicker in its centre with top
631 basement reaching a maximum depth of 5s TWT, and with sediment fill of ~2s TWT which is
632 less than the Liwan sub-basin in the SE China margin. Laterally this inner basin passes into
633 PSH showing a positive ~10 km wide bathymetric expression on the seabed. This high could
634 be considered an analogue to the OMH on the SE China margin. This basement high is
635 bounded by extensional structures, which forms an escarpment of 2s TWT. Seaward, a series
636 of oceanward dipping normal faults is interpreted between 120-150 km (Fig. 7 A, B). The COT
637 is bounded oceanward by an escarpment of the top basement. Seismic definition at the
638 oceanward edge of the COT is partly obscured by volcanic edifices and sills within the post-
639 rift sedimentary sequences. Discontinuous and Moho-like reflections are observed within
640 COT domain, but the quality of seismic data precludes further characterization of deep
641 crustal structures as well as a good definition of syn-rift structures.

642 From 90 to 0 km, the top basement reflector is observed at 6.8 s TWT and another deeper
643 reflector interpreted as the Moho reflector is observed at 9 s TWT, both reflectors are sub-
644 horizontal and parallel. In addition, this domain contains marine magnetic anomalies C10n
645 and C9n. Altogether, this domain is interpreted as oceanic. A sporadic presence of magnetic
646 anomaly C11n is suggested close to the interpreted COB (Fig. 6) by analogy with the SE
647 Chinese side. However, as stated by Briais et al., (1993) the identification of anomaly C11n is
648 not clear on this southern side of the SCS and has also been discarded from the global
649 oceanic magnetic anomaly repository (Seton et al., 2014).

650 The stratigraphic record of the distal Palawan margin remains poorly constrained because of
651 the lack of deep drill holes on the outer margin. Nevertheless, based on seismic facies
652 combined with wells on the shelf, a general stratigraphic framework is suggested.
653 Contrasting with the SE China margin, early post-rift Nido platform carbonates characterized
654 by bright sub-parallel reflections (Fig. 7) (i.e. Nido formation, Steuer et al., 2013) are
655 identified across the proximal part of the profile and suggested on the COT. While syn-rift
656 sedimentary thickness within the inner basin of the NW Palawan margin is significant, in the
657 COT it is reduced to small fault bounded basins (Figs. 7, 8).

658



659

660 **Figure 7: A) Seismic section BGR08-109 interpreted with the major horizons and unconformities**
 661 **(modified from Franke et al., 2011). B) Line drawing of the seismic section C) Depth converted top**

662 basement and comparison in depth between the Moho determined by joint inversion and the
663 Moho determined by gravity anomaly inversion. D) Time depth cross section comparing the Moho
664 predicted from gravity anomaly inversion converted in time, the picked seismic Moho and the joint
665 inversion Moho. E) Lateral variations in basement density along the line 08-109. The blue line
666 corresponds to a density of 2.85 g.cm^{-3} , which is the reference basement density used within the
667 gravity anomaly inversion. PSH: Palawan structural high.

668 **5.3) Gravity inversion of line BGR08-109**

669 We performed gravity inversion and joint inversion on profile 08-109. However, as no
670 reliable Moho reflection is identifiable inboard of kilometre 140 we only perform joint
671 inversion for the COT and oceanic domain (Fig. 7). The Moho from gravity inversion below
672 the inner basin is around 24 km deep, but is slightly shallower within the deepest part of the
673 inner basin. The PSH marks the onset of the main thinning of the continental crust between
674 90 and 155 km. The sharp deepening of the top basement observed on the seismic section
675 oceanward of the PSH corresponds to a gradual shallowing of the Moho over the whole COT.
676 From kilometre 0 to 80 the Moho is almost flat at a depth of 10-11 km forming a crustal layer
677 of 6 to 7 km consistent with its interpreted oceanic nature. The continentward deepening of
678 the Moho around kilometre 90 is confirmed by the basement density estimation resulting
679 from joint inversion of gravity anomaly and TWT seismic data (Fig. 7E). The position of the
680 COB is around kilometre 95 based on the density above 2.85 g.cm^{-3} towards the northwest,
681 whereas continentward within the COT domain the average basement density is only 2.72
682 g.cm^{-3} . This density is low compared to our reference basement density (2.85 g.cm^{-3}). This
683 might be explained in various ways: (1) Rifting developed within an older, deep sedimentary
684 basin, (2) errors in the interpretation of the seismic top basement, or/and Moho reflectors.
685 Indeed, if seismic top basement is picked too shallow, "light" sediments are integrated into
686 the gravity inversion and the average crustal thickness is reduced. Similarly if Moho is
687 picked too deep its average density is reduced.

688

689 **6. Discussion**

690 **6.1) Conjugate margins architecture**

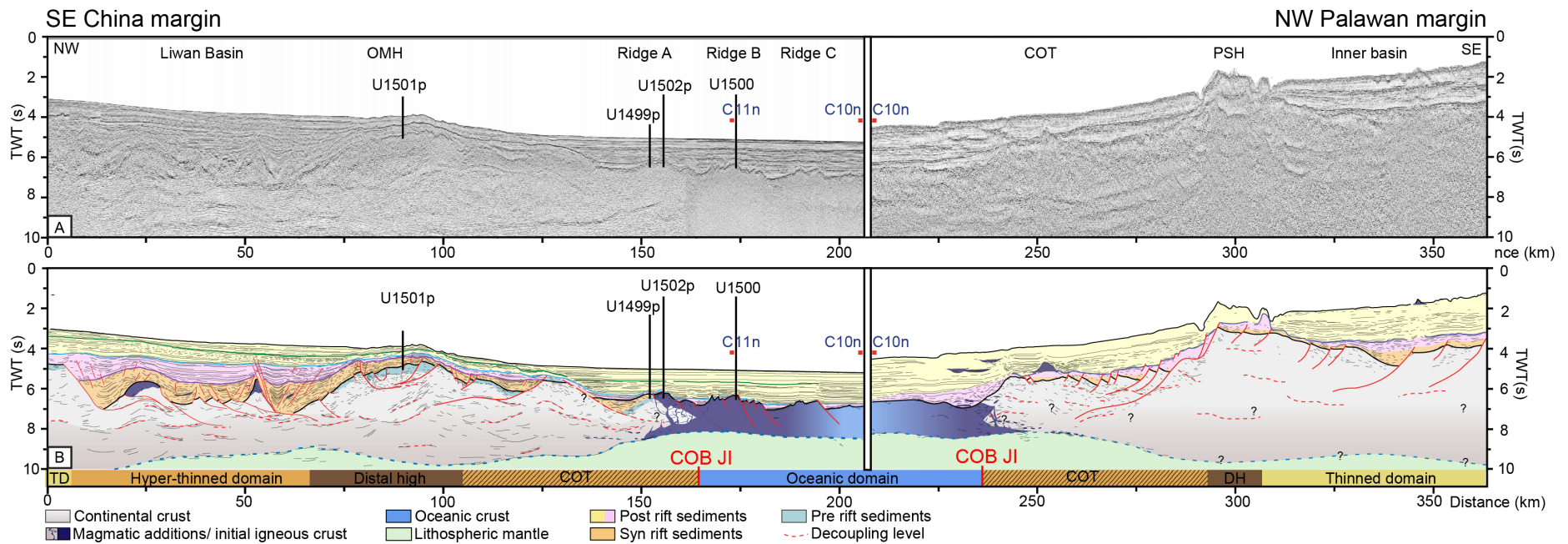
691 The combination of gravity inversion and interpretation of high quality seismic data
692 constrained in critical locations by deep boreholes has allowed us to: (1) confidently tie

693 together the two conjugate margins along the original line of breakup; and (2) amend a
694 definition of structural domains based on crustal structures. The results show that the
695 conjugate segments of the SE China and the NW Palawan margins in pre-breakup time (pre
696 ~30 Ma) together formed a very wide (600 km) rifted zone. This wide rift zone formed a
697 “pinch and swell” crustal architecture (e.g. Savva et al. 2014, Clerc et al. 2018) characterized
698 by a succession of thinned to hyper-thinned basins (e.g. Liwan and Baiyun sub-basins on the
699 SE China margin) separated by basement highs (Fig. 8). The line of final breakup partitioned
700 this wide rift zone into a ~400 km wide margin in the north, and a ~200 km wide margin in
701 the south.

702 At the SCS rifted margins, several studies suggest decoupling between a brittle upper crust
703 and a thick, ductile lower crust (Brune et al., 2017; Savva et al., 2014). This rheological
704 layering of the crust may be caused by several parameters, such as the composition of the
705 crust (more felsic, less mafic, Brune et al., 2017, Nagel and Buck, 2007), structural softening
706 by tectonism, inherited differences in crustal strength (Duretz et al., 2016) and the
707 temperature at Moho level (hotter due to thinner continental lithosphere, Nagel and Buck,
708 2007). Interestingly, within the SE China and NW Palawan margins, based on seismic
709 interpretation we suggest multiple decoupling levels at various depths (e.g., red dashed lines
710 Fig. 3, 25-100 km, Fig.7, 95-160 km). These surfaces may reflect inheritance of pre-rift
711 structural and lithological differences that continue to control weak and strong zones.
712 Variable pre-rift rheological structure is most likely because Paleogene SCS rifting developed
713 within a complex crust that suffered strong deformation during the Mesozoic. The Mesozoic
714 setting is characterized by a convergent system (Holloway, 1981; Klimetz, 1983; Li and Li,
715 2007; Taylor and Hayes, 1983) associated with wide occurrence of granites (J. Li et al., 2014;
716 Savva et al., 2014), volcanoclastic sediments (Nanni et al., 2017), strongly lithified
717 conglomerates (IODP Site U1501), green-schist facies metamorphic rocks (IODP Site U1504
718 (Larsen et al., 2018c), and metasedimentary rocks (Kudrass et al., 1986) dredged or drilled
719 on the SCS margins. Strongly folded Mesozoic sedimentary formations visible on seismic
720 sections (on the Dongsha High, Li et al., 2008), and outcrop on Northern Palawan Island
721 (Faure et al., 1989) are evidence of pre-Cenozoic thrusting and folding within the rift
722 basement below the Tg reflector. The occurrence of multiple decoupling levels at variable
723 depth as observed on seismic data (Fig. 3, 7, 8) may be inherited from a Mesozoic “Andean-

724 type" margin characterized by the former arc, nappes, suture zones and an accretionary
725 wedge.

726 In addition, the joint inversion of gravity modelling highlights variation of densities along the
727 seismic profiles of the SE China margin. On line 1555, the south-eastern part of the OMH has
728 crustal densities in the range of the reference density (2.85 g.cm^{-3}), whereas densities below
729 the Liwan sub-basin are lower. The Liwan sub-basin basement may therefore comprise
730 meta-sediments. By contrast and in accordance with our modelling, numerous structural
731 highs have been interpreted as former Mesozoic plutonic complexes of arc origin and
732 suggesting that major basin bounding faults formed at the edge of Mesozoic intrusive bodies
733 (Savva et al., 2014). Petri et al., (2019) using thermo-mechanical modelling demonstrated
734 the potential importance of such initial heterogeneities in the continental lithosphere on the
735 control of the architecture/development of extensional deformation at rifted margins. In
736 addition to mechanical inheritance, the thermal state of the lithosphere possibly also
737 impacted the rifting of the SCS margins. Indeed, the emplacement of granites between 107-
738 86 Ma (Li et al., 2014) took place less than 50 Ma before the onset of Cenozoic rifting
739 implying a thermally non-equilibrated lithosphere prior to rifting event (McKenzie, 1978).
740 The pre-rift geothermal gradient remains unconstrained, but regarding the fact that the
741 rifting of the SCS developed in a post-orogenic context, it suggests similar heat flow to the
742 one currently observed in the Basin and Range (Western US) $85 \pm 10 \text{ mW/m}^2$ (Blackwell,
743 1983). By comparison the continental heat flow average is much lower $57 \pm 10 \text{ mW/m}^2$
744 (Sclater et al., 1980). This combination of a strongly heterogeneous continental lithosphere
745 combined with elevated thermal conditions probably resulted in a weak pre-rift crust with
746 multiple decoupling zones (interpreted on Figs 3, 7, 8), and a ductile lower crust that framed
747 the final architecture of the margin.



748

749

750

Figure 8: Conjugate seismic cross sections of the SE China-NW Palawan conjugate margins (Larsen et al., 2018e; Franke et al., 2011). A) Un-interpreted section 1555 and 08-109 cropped and merged at the magnetic anomaly C10. B) Conjugate margins seismic interpretation

751 **6.2) Tectonic and magmatic processes shaping the COT and initial igneous crust on the two**
752 **conjugate margins. JI, joint inversion.**

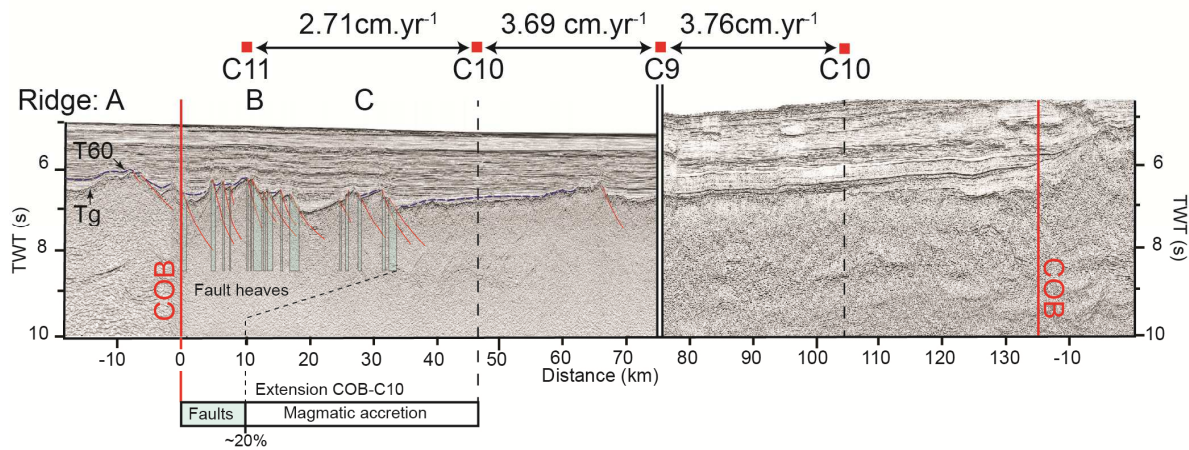
753 The COT along the SE China margin corresponds to a ~60km wide domain from 110 to 170
754 km (Line 1555, Fig.8) where the gravity inversion Moho shallows from 20 to less than 10 km
755 (Figs. 4-5). We interpret a major oceanward dipping low angle extensional fault at 130-155
756 km (Line 1555, Fig.8) offsetting the top basement by 0.8 s (TWT). Over the same interval, the
757 seismic Moho depth abruptly shallows from 9 to 7.5 s (TWT). Hence, we interpret Ridge A
758 (150-160 km) as the hanging-wall block above this major low angle extensional fault. IODP
759 drilling results show that this ridge has a composite nature. At Site U1502 the top basement
760 is formed by late Eocene to early Oligocene altered MORB whereas at Site U1499 pre-
761 and/or syn-rift sediments are found below Tg (Larsen et al. 2018d). Importantly the
762 continental Moho can be followed continuously from the OMH to Ridge A on lines 1555 and
763 1530 showing that Ridge A is at least partly made by highly thinned continental basement
764 (<7km thick), but also affected by breakup magmatism (IODP Site U1502, Larsen et al.,
765 2018b). This interpretation is also supported by the joint inversion of gravity and seismic
766 data on both seismic sections showing that the average basement density at Ridge A is in the
767 range of continental crust (2.85 g.cm^{-3}) (Fig. 4-5).

768 From Ridge B to the end of the seismic line, the joint inversion shows basement density
769 above 2.85 g.cm^{-3} (Fig. 4-5). The domain between ridges A and B is interpreted as the
770 transition from continental crust intruded by magmatic additions (Ridge A) to an entirely
771 mafic igneous crust (Ridge B) and defines a sharp COB. This COB is placed exactly at the same
772 place on the landward side of Ridge B on both seismic lines 1555 and 1530. Line 1530 in this
773 position shows a local, narrow shallowing of the Moho reflector (Fig. 4, around 130 km). The
774 location of the COB, deduced from geophysical data, is consistent with coring results from
775 Site U1500 on Ridge B, which sampled fresh pillow basalts and flows with MORB
776 composition (Stock et al., 2018). As a result, along our profile, the COT is characterized by
777 highly thinned continental crust associated with progressive emplacement of MORB-type
778 magmatic additions. The COB represents the oceanward end of the COT identified with a
779 <4km distance uncertainty by combining gravity modelling, seismic interpretations and core
780 data. Given this relatively sharp boundary a binary definition of COB can be applied (Eagles
781 et al., 2015).

782

783 The oceanic nature of Ridge B is in agreement with the close alignment of magnetic anomaly
784 C11n (30 Ma). Ridges B and C (Fig.9) both show landward block rotation along ocean ward
785 dipping high angle normal faults. These offset the igneous basement to form small half-
786 graben basins filled by post-rift sediments. Sediment fill, however, show poorly developed or
787 no wedge-shaped geometries, and the T60 reflector is not faulted (Fig. 9). These
788 observations suggest that faulting at Ridges B and C occurred while or slightly after basaltic
789 emplacement (C11n, 30Ma) and before the T60 unconformity (This unconformity at Site
790 U1501 corresponds to a sedimentary hiatus from ~24 Ma to ~28 Ma (based on
791 biostratigraphy) or ~30 Ma (based on Sr-isotope stratigraphy) Jian et al. 2019). The rooting
792 level of these normal faults is likely in the deep lower crust (ocean layer 3).

793 On the NW Palawan margin, the Moho shallows oceanward from a depth of 24 to 11 km in
794 about 70 km (Fig. 7). The top basement deformation within the COT is characterized by a set
795 of closely spaced oceanward dipping faults likely rooting in shallow crustal decoupling levels.
796 The fault dip and the structural style may represent the antithetic counter part of the major
797 low angle extensional fault interpreted on the SE China side (km 135; Fig. 8). In contrast with
798 SE China, in the NW Palawan margin the magnetic anomaly C11n (30.0 Ma) is not clearly
799 defined (Briais et al. 1993), but seems to project to the location of the COB on line BGR08-
800 109 (See map Fig.6). However, the first firmly observed magnetic anomaly on both margins
801 is C10n (28.7 Ma) and is located ~45 km from the COB at the SE China margin, and at ~35 km
802 from the COB at the Palawan margin. Another important difference is that this oldest
803 igneous crust off the NW Palawan margin is not faulted, in strong contrast to the faulted
804 Ridges B and C of the SE China margin. Hence, we observed two types of asymmetry: 1) the
805 asymmetrical deformation pattern of the two conjugate highly thinned continental margins
806 (Fig. 8), and 2) the width and morphological asymmetry of the initial igneous crust (Fig. 9)



807

808 **Figure 9: Conjugate seismic cross sections of SE China-NW Palawan conjugate margins cropped and**
 809 **accolated at C9 (~27.97 Ma). The faults heaves are added together in order to get the ratio**
 810 **between tectonic faulting and magmatic extension from COB to C10**

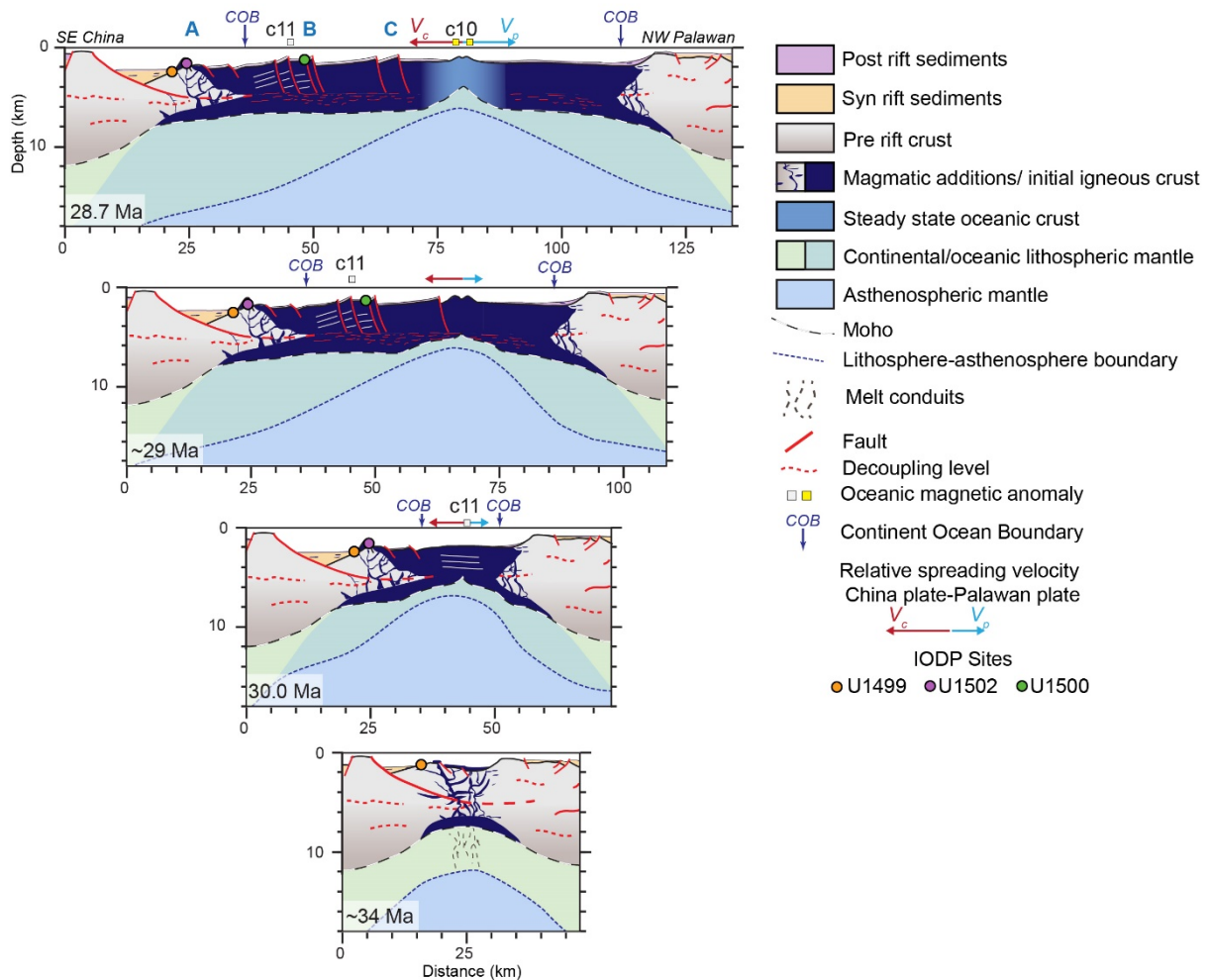
811

812 **6.3 Evolution of the SE China-NW Palawan breakup and initial oceanic accretion**

813 **6.3.1) Stage 1: Eocene-Oligocene boundary: Extreme thinning of the continental** 814 **lithosphere and related magmatism ~34 -30 Ma**

815 The final rifting stage in the SE China-NW Palawan conjugate margins occurs during the
 816 latest Eocene as emphasized by borehole data calibrated with seismic interpretations
 817 (Larsen et al., 2018d). Seismic interpretation suggests that the final extension is caused
 818 mainly by a low angle extensional fault located on the SE China margin (Line 1555, km 130-
 819 155), which enhanced decompression melting. Although in this stage, the continental crust is
 820 less than <10 km thick, the seismic data do not allow the determination of whether the low
 821 angle extensional fault is soling onto an internal crustal level like in the more proximal basins
 822 (e.g. Liwan) or in the uppermost mantle. This structure is interpreted to accommodate
 823 extension triggering an asymmetric crustal architecture at the edge of the COT (Fig. 10),
 824 similarly to that of the hyper-thinned basins observed on both margins (e.g. Liwan sub-
 825 basin). Overall and similarly to the observation from the Red Sea breakup (Ligi et al., 2018),
 826 the extreme lithospheric thinning resulted in the initiation of MORB magmatism before
 827 continental rupture. From seismic observations and IODP drilling, we interpret Ridge A as
 828 representing the last continental rotated fault block strongly overprinted by magmatic
 829 additions emplaced through the whole residual crust. Basalts and the first (~5m) early
 830 Oligocene sediments of Site U1502 show significant hydrothermal alteration. This alteration

831 constrains the timing of magmatic activity and faulting to early Oligocene time (34-30 Ma).
 832 The concomitant faulting and magmatic activity results in the continental crust tapering with
 833 rapid but likely progressive replacement by magmatic rocks. The COTs on both margins
 834 appear quite narrow and formed most likely in less than 4 Ma by faulting, diking, intrusions
 835 and building of volcanic edifices (Larsen et al., 2018d).



836

837 **Figure 10: Tectono-magmatic evolutionary model illustrating the breakup and the early seafloor**
 838 **spreading at the SE China-NW Palawan conjugate margins. The initial asymmetric spreading and**
 839 **the strong interplay between faulting and magmatism are highlighted.**

840 **6.3.2) Stages 2 and 3: Formation of initial igneous crust ~30 – 29 Ma**

841 Seismic interpretation, borehole data and gravity modelling highlight the asymmetry in
 842 width and morphology of the initial igneous crust between SE China and NW Palawan. The
 843 morphology and ages of the T60 reflector (Fig. 9) indicate that this asymmetry is produced
 844 within a short time interval after the formation of the igneous crust and therefore likely

845 generated during seafloor accretion. The calculated half-spreading rate between C11 and
846 C10 is 2.71 cm.yr^{-1} and accelerates to 3.69 cm.yr^{-1} between C10 and C9 on the SE China side.
847 C11 is not clearly identified on the NW Palawan margin (Fig. 6), therefore half-spreading rate
848 cannot be determined, but as the distance is smaller between the COB and C10 compared to
849 the SE China side the half-spreading rate is slower on the NW Palawan, implying that initial
850 spreading was asymmetric. However, the sum of the fault heaves between the COB and C10
851 on the SE China side represent a minimum of 20% of the total distance while the remaining
852 80% are caused by magmatic accretion (Fig. 9). If we remove the 20% caused by extensional
853 faulting to the distance between the COB and C10 on the SE China margin, the distance
854 between the COB and C10 becomes similar on both margins (Fig. 9). An explanation to this
855 asymmetry could be related to a southward jump of seafloor spreading axis, which would be
856 consistent with the younger igneous crust observed on the conjugate Palawan margin.
857 However, all faults on the SE China margin dip oceanward and there is no seismic evidence
858 of an extinct axis (e.g., a symmetric graben structure) making the axis jump hypothesis
859 unlikely. This analysis supports a southward migration of the initial spreading centre with
860 tectonic extension within the trailing edge (on SE China side compared to the mobile
861 Palawan block see Stein et al., 1977).

862

863 The stage of asymmetric spreading ended around C10n when spreading rate became
864 symmetric without normal faulting, and accelerated to $\sim 3.7 \text{ cm.yr}^{-1}$ (Fig. 9). Asymmetric
865 seafloor spreading is commonly observed on oceanic basins (Müller et al., 2008), however
866 the 20% observed on our example is anomalously high. One reason for an initial asymmetric
867 spreading stage might be related to a temporary, preferred shape of asthenospheric
868 upwelling, less inclined towards the northwest inducing a faster extension of the trailing
869 edge (Stein et al., 1977). This asthenospheric upwelling could be related to the asymmetric
870 late stage of rifting (e.g. faulting of Ridge A) resulting in a migration of the deformation and
871 magmatism (Brune et al., 2014). We interpret the phase between $\sim 30 \text{ Ma}$ and C10 as the
872 incipient building of a symmetric steady state oceanic accretion.

873 **6.3.3) Stage 4: Steady-state oceanic accretion $\sim 28.7 \text{ Ma}$ onward**

874 Between anomalies C10n and C9n the half spreading rate are similar on both side (3.69
875 cm.yr^{-1} on the SE China margin and 3.76 cm.yr^{-1} on the NW Palawan Fig. 9) suggesting a

876 steady-state symmetric oceanic crust accretion (Fig. 10). Oceanward of C10n the oceanic
877 seismic facies are very similar on both sides of the SCS with little faulting of the top of the
878 oceanic crust suggesting a magma dominated accretion. The symmetric steady state oceanic
879 spreading system starts around C10n (28.7 Ma) (Fig. 10; Briais et al., 1993) and corresponds
880 to the stabilization of the plate boundary until the southward jump identified at the C6b
881 (~23 Ma) (Briais et al., 1993).

882

883 **7. Conclusion**

884 This study investigated the architecture of SE China-NW Palawan conjugate margins within
885 the eastern SCS sub-basin using information from new IODP drill cores, high quality seismic
886 sections and modelling of the free-air gravity anomalies. The localisation of the COB is
887 accurately determined by gravity inversion and is in agreement with the IODP drill cores and
888 seismic profiles.

889 On the continental rifted margins, gravity inversion highlights variations of crustal densities
890 and seismic interpretations suggest multiple decoupling levels which influence the
891 extensional deformation style. Such crustal heterogeneities are considered to be related to
892 the structural, compositional and thermal inheritance from the Mesozoic convergence
893 history. Our study unravels the architecture of the COT on the SE China-NW Palawan
894 conjugate margins. Both COTs show normal faults and hyperthinned crust (<15 km) over
895 equivalent distances until the COB, however, the final crustal thinning is suggested to be
896 accommodated by a major low angle extensional fault locate on the SE China margin. The
897 strong lithospheric thinning induced the emplacement of MORB magmatic additions within
898 the COT. This initial magmatic activity was concomitant with continued deformation of
899 continental crust until the COB. Oceanward of the COB the initial igneous crust along the two
900 conjugate margins is asymmetric in both width and morphology. These observations
901 constrained by seismic stratigraphy, suggest that initial spreading rate was faster on the SE
902 China side before oceanic magnetic anomaly C10n (28.7 Ma) by which time the spreading
903 ridge generated oceanic crust at symmetric rates. The initial asymmetry pictures the
904 incipient building of a steady state oceanic spreading and could be due to oriented
905 asthenospheric upwelling inherited from the asymmetric late rifting stage.

906

907 **Acknowledgments**

908 This research used data provided by the International Ocean Discovery Program (IODP). We
909 thanks the participants to IODP Expedition 367-368 as well as the captains and crew of the
910 Joides Resolution. We acknowledge IODP France for post cruise support. Funding for this
911 research and access to industrial seismic and borehole data were provided by Total SA R&D
912 (J.N. Ferry). We are grateful to the Editor Tiago Alves. Chao Lei, William Bosworth and two
913 anonymous reviewers are thanked for their helpful suggestions and comments.
914

915 **References**

- 916 Alvey, A., Gaina, C., Kuszniir, N.J., Torsvik, T.H., 2008. Integrated crustal thickness mapping and plate
917 reconstructions for the high Arctic. *Earth Planet. Sci. Lett.* 274, 310–321.
918 <https://doi.org/10.1016/j.epsl.2008.07.036>
- 919 Amante, C., Eakins, B.W., 2009. ETOPO1 1 Arc-Minute Global Relief Model: Procedures, Data Sources
920 and Analysis. <https://doi.org/10.7289/V5C8276M>
- 921 Arfai, J., Franke, D., Gaedicke, C., Lutz, R., Schnabel, M., Ladage, S., Berglar, K., Aurelio, M., Montano,
922 J., Pellejera, N., 2011. Geological evolution of the West Luzon Basin (South China Sea,
923 Philippines). *Mar. Geophys. Res.* 32, 349–362. <https://doi.org/10.1007/s11001-010-9113-x>
- 924 Barckhausen, U., Engels, M., Franke, D., Ladage, S., Pubellier, M., 2014. Evolution of the South China
925 Sea: Revised ages for breakup and seafloor spreading. *Mar. Pet. Geol.* 58, 599–611.
926 <https://doi.org/10.1016/j.marpetgeo.2014.02.022>
- 927 Birch, F., 1961. The velocity of compressional waves in rocks to 10 kilobars, part 2. *Elastic Prop.*
928 *Equations State* 66, 91–116. <https://doi.org/10.1029/SP026p0091>
- 929 Blackwell, D.D., 1983. Heat flow in the Northern Basin and Range Province, in: *The Role of Heat in the*
930 *Development of Energy and Mineral Resources in the Northern Basin and Range Province.* pp.
931 81–93.
- 932 Boillot, G., Winterer, E.L., Meyer, A.W. (Eds.), 1987. *Proceedings of the Ocean Drilling Program, 103*
933 *Initial Reports, Proceedings of the Ocean Drilling Program. Ocean Drilling Program.*
934 <https://doi.org/10.2973/odp.proc.ir.103.1987>
- 935 Briaies, A., Patriat, P., Tapponnier, P., 1993. Updated interpretation of magnetic anomalies and
936 seafloor spreading stages in the south China Sea: Implications for the Tertiary tectonics of
937 Southeast Asia. *J. Geophys. Res. Solid Earth* 98, 6299–6328. <https://doi.org/10.1029/92JB02280>
- 938 Brocher, T.M., 2005. Empirical Relations between Elastic Wavespeeds and Density in the Earth's
939 Crust. *Bull. Seismol. Soc. Am.* 95, 2081–2092. <https://doi.org/10.1785/0120050077>
- 940 Brune, S., Heine, C., Clift, P.D., Pérez-Gussinyé, M., 2017. Rifted margin architecture and crustal
941 rheology: Reviewing Iberia-Newfoundland, Central South Atlantic, and South China Sea. *Mar.*
942 *Pet. Geol.* 79, 257–281. <https://doi.org/10.1016/j.marpetgeo.2016.10.018>
- 943 Brune, S., Heine, C., Pérez-Gussinyé, M., Sobolev, S. V., 2014. Rift migration explains continental
944 margin asymmetry and crustal hyper-extension. *Nat. Commun.* 5, 4014.
945 <https://doi.org/10.1038/ncomms5014>
- 946 Cameselle, A.L., Ranero, C.R., Franke, D., Barckhausen, U., 2017. The continent-ocean transition on
947 the northwestern South China Sea. *Basin Res.* 29, 73–95. <https://doi.org/10.1111/bre.12137>
- 948 Carlson, R.L., Raskin, G.S., 1984. Density of the ocean crust. *Nature* 311, 555–558.

949 <https://doi.org/10.1038/309126a0>

950 Chappell, A.R., Kusznir, N.J., 2008. Three-dimensional gravity inversion for Moho depth at rifted
951 continental margins incorporating a lithosphere thermal gravity anomaly correction. *Geophys. J.*
952 *Int.* 174, 1–13. <https://doi.org/10.1111/j.1365-246X.2008.03803.x>

953 Childress, L., 2019. Expedition 368X Preliminary Report: South China Sea Rifted Margin, International
954 Ocean Discovery Program Preliminary Report. International Ocean Discovery Program.
955 <https://doi.org/10.14379/iodp.pr.368X.2019>

956 Clerc, C., Jolivet, L., Ringenbach, J.C., 2015. Ductile extensional shear zones in the lower crust of a
957 passive margin. *Earth Planet. Sci. Lett.* 431, 1–7. <https://doi.org/10.1016/j.epsl.2015.08.038>

958 Clerc, C., Ringenbach, J.C., Jolivet, L., Ballard, J.F., 2018. Rifted margins: Ductile deformation,
959 boudinage, continentward-dipping normal faults and the role of the weak lower crust.
960 *Gondwana Res.* 53, 20–40. <https://doi.org/10.1016/j.gr.2017.04.030>

961 Clift, P.D., Brune, S., Quinteros, J., 2015. Climate changes control offshore crustal structure at South
962 China Sea continental margin. *Earth Planet. Sci. Lett.* 420, 66–72.
963 <https://doi.org/10.1016/j.epsl.2015.03.032>

964 Cowie, L., Angelo, R.M., Kusznir, N., Manatschal, G., Horn, B., 2017. Structure of the ocean–continent
965 transition, location of the continent–ocean boundary and magmatic type of the northern
966 Angolan margin from integrated quantitative analysis of deep seismic reflection and gravity
967 anomaly data. *Geol. Soc. London, Spec. Publ.* 438, 159–176. <https://doi.org/10.1144/SP438.6>

968 Cullen, A., Reemst, P., Henstra, G., Gozzard, S., Ray, A., 2010. Rifting of the South China Sea: new
969 perspectives. *Pet. Geosci.* 16, 273–282. <https://doi.org/10.1144/1354-079309-908>

970 Curray, J.R., 1980. The Ipod Programme on Passive Continental Margins. *Philos. Trans. R. Soc. A*
971 *Math. Phys. Eng. Sci.* 294, 17–33. <https://doi.org/10.1098/rsta.1980.0008>

972 Davis, J.K., Lavier, L.L., 2017. Influences on the development of volcanic and magma-poor
973 morphologies during passive continental rifting. *Geosphere* 13, 1524–1540.
974 <https://doi.org/10.1130/GES01538.1>

975 de Boer, J., Odom, L.A., Ragland, P.C., Snider, F.G., Tilford, N.R., 1980. The Bataan orogene: Eastward
976 subduction, tectonic rotations, and volcanism in the western Pacific (Philippines).
977 *Tectonophysics* 67, 251–282. [https://doi.org/10.1016/0040-1951\(80\)90270-X](https://doi.org/10.1016/0040-1951(80)90270-X)

978 Dewey, J.F., Bird, J.M., 1970. Mountain belts and the new global tectonics. *J. Geophys. Res.* 75, 2625–
979 2647. <https://doi.org/10.1029/JB075i014p02625>

980 Ding, W., Schnabel, M., Franke, D., Ruan, A., Wu, Z., 2012. Crustal Structure across the Northwestern
981 Margin of South China Sea: Evidence for Magma-poor Rifting from a Wide-angle Seismic Profile.
982 *Acta Geol. Sin. - English Ed.* 86, 854–866. <https://doi.org/10.1111/j.1755-6724.2012.00711.x>

983 Ding, W., Sun, Z., Dadd, K., Fang, Y., Li, J., 2018. Structures within the oceanic crust of the central
984 South China Sea basin and their implications for oceanic accretionary processes. *Earth Planet.*
985 *Sci. Lett.* 488, 115–125. <https://doi.org/10.1016/j.epsl.2018.02.011>

986 Doo, W. Bin, Hsu, S.K., Armada, L., 2015. New magnetic anomaly map of the east asia with some
987 preliminary tectonic interpretations. *Terr. Atmos. Ocean. Sci.* 26, 73–81.
988 [https://doi.org/10.3319/TAO.2014.08.19.07\(GRT\)](https://doi.org/10.3319/TAO.2014.08.19.07(GRT))

989 Duretz, T., Petri, B., Mohn, G., Schmalholz, S.M., Schenker, F.L., Müntener, O., 2016. The importance
990 of structural softening for the evolution and architecture of passive margins. *Sci. Rep.* 6, 1–7.
991 <https://doi.org/10.1038/srep38704>

- 992 Eagles, G., Pérez-Díaz, L., Scarselli, N., 2015. Getting over continent ocean boundaries. *Earth-Science*
993 *Rev.* 151, 244–265. <https://doi.org/10.1016/j.earscirev.2015.10.009>
- 994 Falvey, D.A., 1974. The development of continental margins in plate tectonic theory. *APPEA J.* 14, 95.
995 <https://doi.org/10.1071/AJ73012>
- 996 Faure, M., Marchadier, Y., Rangin, C., 1989. Pre-Eocene Synmetamorphic Structure in the Mindoro-
997 Romblon-Palawan Area, West Philippines, and implications for the history of southeast Asia.
998 *Tectonics* 8, 963–979. <https://doi.org/10.1029/TC008i005p00963>
- 999 Fontaine, H., 1979. Note on the geology of the Calamian Islands, North Palawan, Philippines. *CCOP*
1000 *Newsletter*, Vol. 6, No.2
- 1001 Fournier, F.T., Borgomano, J., Montaggioni, L.F., 2005. Development patterns and controlling factors
1002 of Tertiary carbonate buildups : Insights from high-resolution 3D seismic and well data in the
1003 Malampaya gas field (Offshore Palawan, Philippines). *Sediment. Geol.* 175, 189–215.
1004 <https://doi.org/10.1016/j.sedgeo.2005.01.009>
- 1005 Franke, D., Barckhausen, U., Baristead, N., Engels, M., Ladage, S., Lutz, R., Montano, J., Pellejera, N.,
1006 Ramos, E.G., Schnabel, M., 2011. The continent-ocean transition at the southeastern margin of
1007 the South China Sea. *Mar. Pet. Geol.* 28, 1187–1204.
1008 <https://doi.org/10.1016/j.marpetgeo.2011.01.004>
- 1009 Franke, D., Savva, D., Pubellier, M., Steuer, S., Mouly, B., Auxietre, J.-L., Meresse, F., Chamot-Rooke,
1010 N., 2014. The final rifting evolution in the South China Sea. *Mar. Pet. Geol.* 58, 704–720.
1011 <https://doi.org/10.1016/j.marpetgeo.2013.11.020>
- 1012 Gao, J., Wu, S., McIntosh, K., Mi, L., Yao, B., Chen, Z., Jia, L., 2015. The continent-ocean transition at
1013 the mid-northern margin of the South China Sea. *Tectonophysics* 654, 1–19.
1014 <https://doi.org/10.1016/j.tecto.2015.03.003>
- 1015 Ge, J.W., Zhu, X.M., Zhang, X.T., Jones, B.G., Yu, F.S., Niu, Z.C., Li, M., 2017. Tectono-stratigraphic
1016 evolution and hydrocarbon exploration in the Eocene Southern Lufeng Depression, Pearl River
1017 Mouth Basin, South China Sea. *Aust. J. Earth Sci.* 64, 931–956.
1018 <https://doi.org/10.1080/08120099.2017.1370613>
- 1019 Gee, J.S., Kent, D. V., 2007. Source of Oceanic Magnetic Anomalies and the Geomagnetic Polarity
1020 Timescale, in: *Treatise on Geophysics*. pp. 455–475. [https://doi.org/10.1016/B978-044452748-](https://doi.org/10.1016/B978-044452748-6.00097-3)
1021 [6.00097-3](https://doi.org/10.1016/B978-044452748-6.00097-3)
- 1022 Gozzard, S., Kuszniir, N., Franke, D., Cullen, A., Reemst, P., Henstra, G., 2019. South China Sea crustal
1023 thickness and oceanic lithosphere distribution from satellite gravity inversion. *Pet. Geosci.* 25,
1024 112–128. <https://doi.org/10.1144/petgeo2016-162>
- 1025 Haizhang, Y., Ying, C., Mo, J., Yinxue, H., Longying, W., Xuan, H., 2017. Structural evolution
1026 differences and the significance for oil and gas exploration in the deep water area of the Pearl
1027 River Mouth Basin. *China Pet. Explor.* 22, 1–11.
- 1028 Harkin, C., Kuszniir, N., Tugend, J., Manatschal, G., McDermott, K., 2019. Evaluating magmatic
1029 additions at a magma-poor rifted margin: An East Indian case study. *Geophys. J. Int.*
1030 <https://doi.org/10.1093/gji/ggz007>
- 1031 Hayes, D.E., Nissen, S.S., 2005. The South China sea margins: Implications for rifting contrasts. *Earth*
1032 *Planet. Sci. Lett.* 237, 601–616. <https://doi.org/10.1016/j.epsl.2005.06.017>
- 1033 Heezen, B.C., 1960. The Rift in the Ocean Floor. *Sci. Am.* 203, 98–110.
1034 <https://doi.org/10.1038/scientificamerican1060-98>

- 1035 Holloway, N., 1981. The North Palawan Block, Philippines: its relation to the Asian Mainland and its
1036 role in the evolution of the South China Sea. *Bull. Geol. Soc. Malaysia* 14, 19–58.
- 1037 Huismans, R., Beaumont, C., 2011. Depth-dependent extension, two-stage breakup and cratonic
1038 underplating at rifted margins. *Nature* 473, 74–78. <https://doi.org/10.1038/nature09988>
- 1039 Jian, Z., Larsen, H.C., Alvarez Zariqian, C.A., Sun, Z., Stock, J.M., Klaus, A., Boaga, J., Bowden, S.A.,
1040 Briais, A., Chen, Y., Cukur, D., Dadd, K.A., Ding, W., Dorais, M.J., Ferré, E.C., Ferreira, F.,
1041 Furusawa, A., Gewecke, A.J., Hinojosa, J.L., Höfig, T.W., Hsiung, K.H., Huang, B., Huang, E.,
1042 Huang, X.L., Jiang, S., Jin, H., Johnson, B.G., Kurzawski, R.M., Lei, C., Li, B., Li, L., Li, Y., Lin, J., Liu,
1043 C., Liu, C., Liu, Z., Luna, A., Lupi, C., McCarthy, A.J., Mohn, G., Ningthoujam, L.S., Nirrengarten,
1044 M., Osono, N., Peate, D.W., Persaud, P., Qiu, N., Robinson, C.M., Satolli, S., Sauermilch, I.,
1045 Schindlbeck, J.C., Skinner, S.M., Straub, S.M., Su, X., Tian, L., van der Zwan, F.M., Wan, S., Wu,
1046 H., Xiang, R., Yadav, R., Yi, L., Zhang, C., Zhang, J., Zhang, Y., Zhao, N., Zhong, G., Zhong, L., 2018.
1047 Site U1505, in: *Proceedings of the International Ocean Discovery Program Volume 367/368*.
1048 <https://doi.org/10.14379/iodp.proc.367368.109.2018>
- 1049 Jian, Z., Jin, H., Kaminski, M.A., Ferreira, F., Li, B., Yu, P.-S., 2019. Discovery of the marine Eocene in
1050 the northern South China Sea. *Natl. Sci. Rev.* <https://doi.org/10.1093/nsr/nwz084>
- 1051 Karig, D.E., 1983. Accreted terranes in the northern part of the Philippine Archipelago. *Tectonics* 2,
1052 211–236. <https://doi.org/10.1029/TC002i002p00211>
- 1053 Klimetz, M.P., 1983. Speculations on the Mesozoic Plate tectonic evolution of eastern China 2, 139–
1054 166. <https://doi.org/10.1029/TC002i002p00139>
- 1055 Kudrass, H.R., Wiedicke, M., Cepek, P., Kreuzer, H., Müller, P., 1986. Mesozoic and Cainozoic rocks
1056 dredged from the South China Sea (Reed Bank area) and Sulu Sea and their significance for
1057 plate-tectonic reconstructions. *Mar. Pet. Geol.* 3, 19–30. [https://doi.org/10.1016/0264-8172\(86\)90053-X](https://doi.org/10.1016/0264-8172(86)90053-X)
- 1059 Kuzsnir, N.J., Roberts, A.M., Alvey, A.D., 2018. Crustal structure of the conjugate Equatorial Atlantic
1060 Margins, derived by gravity anomaly inversion. *Geol. Soc. London, Spec. Publ.* SP476.5.
1061 <https://doi.org/10.1144/SP476.5>
- 1062 Larsen, H.C., Jian, Z., Alvarez Zariqian, C.A., Sun, Z., Stock, J.M., Klaus, A., Boaga, J., Bowden, S.A.,
1063 Briais, A., Chen, Y., Cukur, D., Dadd, K.A., Ding, W., Dorais, M.J., Ferré, E.C., Ferreira, F.,
1064 Furusawa, A., Gewecke, A.J., Hinojosa, J.L., Höfig, T.W., Hsiung, K.H., Huang, B., Huang, E.,
1065 Huang, X.L., Jiang, S., Jin, H., Johnson, B.G., Kurzawski, R.M., Lei, C., Li, B., Li, L., Li, Y., Lin, J., Liu,
1066 C., Liu, C., Liu, Z., Luna, A., Lupi, C., McCarthy, A.J., Mohn, G., Ningthoujam, L.S., Nirrengarten,
1067 M., Osono, N., Peate, D.W., Persaud, P., Qiu, N., Robinson, C.M., Satolli, S., Sauermilch, I.,
1068 Schindlbeck, J.C., Skinner, S.M., Straub, S.M., Su, X., Tian, L., van der Zwan, F.M., Wan, S., Wu,
1069 H., Xiang, R., Yadav, R., Yi, L., Zhang, C., Zhang, J., Zhang, Y., Zhao, N., Zhong, G., Zhong, L.,
1070 2018a. Site U1501, in: *Proceedings of the International Ocean Discovery Program Volume*
1071 *367/368*. <https://doi.org/10.14379/iodp.proc.367368.105.2018>
- 1072 Larsen, H.C., Jian, Z., Alvarez Zariqian, C.A., Sun, Z., Stock, J.M., Klaus, A., Boaga, J., Bowden, S.A.,
1073 Briais, A., Chen, Y., Cukur, D., Dadd, K.A., Ding, W., Dorais, M.J., Ferré, E.C., Ferreira, F.,
1074 Furusawa, A., Gewecke, A.J., Hinojosa, J.L., Höfig, T.W., Hsiung, K.H., Huang, B., Huang, E.,
1075 Huang, X.L., Jiang, S., Jin, H., Johnson, B.G., Kurzawski, R.M., Lei, C., Li, B., Li, L., Li, Y., Lin, J., Liu,
1076 C., Liu, C., Liu, Z., Luna, A., Lupi, C., McCarthy, A.J., Mohn, G., Ningthoujam, L.S., Nirrengarten,
1077 M., Osono, N., Peate, D.W., Persaud, P., Qiu, N., Robinson, C.M., Satolli, S., Sauermilch, I.,
1078 Schindlbeck, J.C., Skinner, S.M., Straub, S.M., Su, X., Tian, L., van der Zwan, F.M., Wan, S., Wu,
1079 H., Xiang, R., Yadav, R., Yi, L., Zhang, C., Zhang, J., Zhang, Y., Zhao, N., Zhong, G., Zhong, L.,
1080 2018b. Site U1502, in: *Proceedings of the International Ocean Discovery Program Volume*

- 1081 367/368. <https://doi.org/10.14379/iodp.proc.367368.106.2018>
- 1082 Larsen, H.C., Jian, Z., Alvarez Zarikian, C.A., Sun, Z., Stock, J.M., Klaus, A., Boaga, J., Bowden, S.A.,
1083 Briaais, A., Chen, Y., Cukur, D., Dadd, K.A., Ding, W., Dorais, M.J., Ferré, E.C., Ferreira, F.,
1084 Furusawa, A., Gewecke, A.J., Hinojosa, J.L., Höfig, T.W., Hsiung, K.H., Huang, B., Huang, E.,
1085 Huang, X.L., Jiang, S., Jin, H., Johnson, B.G., Kurzawski, R.M., Lei, C., Li, B., Li, L., Li, Y., Lin, J., Liu,
1086 C., Liu, C., Liu, Z., Luna, A., Lupi, C., McCarthy, A.J., Mohn, G., Ningthoujam, L.S., Nirrengarten,
1087 M., Osono, N., Peate, D.W., Persaud, P., Qiu, N., Robinson, C.M., Satolli, S., Sauermilch, I.,
1088 Schindlbeck, J.C., Skinner, S.M., Straub, S.M., Su, X., Tian, L., van der Zwan, F.M., Wan, S., Wu,
1089 H., Xiang, R., Yadav, R., Yi, L., Zhang, C., Zhang, J., Zhang, Y., Zhao, N., Zhong, G., Zhong, L.,
1090 2018c. Site U1504, in: Proceedings of the International Ocean Discovery Program Volume
1091 367/368. <https://doi.org/10.14379/iodp.proc.367368.108.2018>
- 1092 Larsen, H.C., Mohn, G., Nirrengarten, M., Sun, Z., Stock, J., Jian, Z., Klaus, A., Alvarez-Zarikian, C.A.,
1093 Boaga, J., Bowden, S.A., Briaais, A., Chen, Y., Cukur, D., Dadd, K., Ding, W., Dorais, M., Ferré, E.C.,
1094 Ferreira, F., Furusawa, A., Gewecke, A., Hinojosa, J., Höfig, T.W., Hsiung, K.H., Huang, B., Huang,
1095 E., Huang, X.L., Jiang, S., Jin, H., Johnson, B.G., Kurzawski, R.M., Lei, C., Li, B., Li, L., Li, Y., Lin, J.,
1096 Liu, C., Liu, C., Liu, Z., Luna, A.J., Lupi, C., McCarthy, A., Ningthoujam, L., Osono, N., Peate, D.W.,
1097 Persaud, P., Qiu, N., Robinson, C., Satolli, S., Sauermilch, I., Schindlbeck, J.C., Skinner, S., Straub,
1098 S., Su, X., Su, C., Tian, L., van der Zwan, F.M., Wan, S., Wu, H., Xiang, R., Yadav, R., Yi, L., Yu, P.S.,
1099 Zhang, C., Zhang, J., Zhang, Y., Zhao, N., Zhong, G., Zhong, L., 2018d. Rapid transition from
1100 continental breakup to igneous oceanic crust in the South China Sea. *Nat. Geosci.* 11, 782–789.
1101 <https://doi.org/10.1038/s41561-018-0198-1>
- 1102 Larsen, H.C., Sun, Z., Stock, J.M., Jian, Z., Alvarez Zarikian, C.A., Klaus, A., Boaga, J., Bowden, S.A.,
1103 Briaais, A., Chen, Y., Cukur, D., Dadd, K.A., Ding, W., Dorais, M.J., Ferré, E.C., Ferreira, F.,
1104 Furusawa, A., Gewecke, A.J., Hinojosa, J.L., Höfig, T.W., Hsiung, K.H., Huang, B., Huang, E.,
1105 Huang, X.L., Jiang, S., Jin, H., Johnson, B.G., Kurzawski, R.M., Lei, C., Li, B., Li, L., Li, Y., Lin, J., Liu,
1106 C., Liu, C., Liu, Z., Luna, A., Lupi, C., McCarthy, A.J., Mohn, G., Ningthoujam, L.S., Nirrengarten,
1107 M., Osono, N., Peate, D.W., Persaud, P., Qiu, N., Robinson, C.M., Satolli, S., Sauermilch, I.,
1108 Schindlbeck, J.C., Skinner, S.M., Straub, S.M., Su, X., Tian, L., van der Zwan, F.M., Wan, S., Wu,
1109 H., Xiang, R., Yadav, R., Yi, L., Zhang, C., Zhang, J., Zhang, Y., Zhao, N., Zhong, G., Zhong, L.,
1110 2018e. Expedition 367/368 summary, in: Proceedings of the International Ocean Discovery
1111 Program Volume 367/368. <https://doi.org/10.14379/iodp.proc.367368.101.2018>
- 1112 Le Pourhiet, L., Chamot-Rooke, N., Delescluse, M., May, D.A., Watremez, L., Pubellier, M., 2018.
1113 Continental break-up of the South China Sea stalled by far-field compression. *Nat. Geosci.*
1114 <https://doi.org/10.1038/s41561-018-0178-5>
- 1115 Lei, C., Alves, T.M., Ren, J., Pang, X., Yang, L., Liu, J., 2019. Depositional architecture and structural
1116 evolution of a region immediately inboard of the locus of continental. *Geol. Soc. Am.* 1–16.
1117 <https://doi.org/10.1130/B35001.1/4637903/b35001.pdf>
- 1118 Lei, C., Ren, J., 2016. Hyper-extended rift systems in the Xisha Trough, northwestern South China Sea:
1119 Implications for extreme crustal thinning ahead of a propagating ocean. *Mar. Pet. Geol.* 77,
1120 846–864. <https://doi.org/10.1016/j.marpetgeo.2016.07.022>
- 1121 Lei, C., Ren, J., Pang, X., Chao, P. and Han, X., 2018. Continental rifting and sediment infill in the distal
1122 part of the northern South China Sea in the Western Pacific region: Challenge on the present-
1123 day models for the passive margins. *Marine and Petroleum Geology*, 93: 166-181.
- 1124 Lester, R., Van Avendonk, H.J.A., McIntosh, K., Lavier, L., Liu, C.S., Wang, T.K., Wu, F., 2014. Rifting
1125 and magmatism in the northeastern South China Sea from wide-angle tomography and seismic
1126 reflection imaging. *J. Geophys. Res. Solid Earth* 119, 2305–2323.
1127 <https://doi.org/10.1002/2013JB010639>

- 1128 Li, C.-F., Lin, J., Kulhanek, D.K., Williams, T., Bao, R., Briais, A., Brown, E.A., Chen, Y., Clift, P.D.,
1129 Colwell, F.S., Dadd, K.A., Ding, W.-W., Hernández-Almeida, I., Huang, X.-L., Hyun, S., Jiang, T.,
1130 Koppers, A.A.P., Li, Q., Liu, C., Liu, Q., Liu, Z., Nagai, R.H., Peleo-Alampay, A., Su, X., Sun, Z.,
1131 Tejada, M.L.G., Trinh, H.S., Yeh, Y.-C., Zhang, C., Zhang, F., Zhang, G.-L., Zhao, X., 2015.
1132 Expedition 349 summary, in: Proceedings of the International Ocean Discovery Program Volume
1133 349. <https://doi.org/10.14379/iodp.proc.349.101.2015>
- 1134 Li, C.-F., Xu, X., Lin, J., Sun, Z., Zhu, J., Yao, Y., Zhao, X., Liu, Q., Kulhanek, D.K., Wang, J., Song, T., Zhao,
1135 J., Qiu, N., Guan, Y., Zhou, Z., Williams, T., Bao, R., Briais, A., Brown, E.A., Chen, Y., Clift, P.D.,
1136 Colwell, F.S., Dadd, K.A., Ding, W., Almeida, I.H., Huang, X.-L., Hyun, S., Jiang, T., Koppers, A.A.P.,
1137 Li, Q., Liu, C., Liu, Z., Nagai, R.H., Peleo-Alampay, A., Su, X., Tejada, M.L.G., Trinh, H.S., Yeh, Y.-C.,
1138 Zhang, C., Zhang, F., Zhang, G.-L., 2014. Ages and magnetic structures of the South China Sea
1139 constrained by deep tow magnetic surveys and IODP Expedition 349. *Geochemistry, Geophys.*
1140 *Geosystems* 15, 4958–4983. <https://doi.org/10.1002/2014GC005567>
- 1141 Li, C., Zhou, Z., Hao, H., Chen, B., Chen, H., Wang, J., Wu, J., 2008. Late Mesozoic tectonic structure
1142 and evolution along the present-day northeastern South China Sea continental margin. *J. Asian*
1143 *Earth Sci.* 31, 546–561. <https://doi.org/10.1016/j.jseas.2007.09.004>
- 1144 Li, J., Zhang, Y., Dong, S., Johnston, S.T., 2014. Cretaceous tectonic evolution of South China: A
1145 preliminary synthesis. *Earth-Science Rev.* 134, 98–136.
1146 <https://doi.org/10.1016/j.earscirev.2014.03.008>
- 1147 Li, Z., Li, X.-H., 2007. Formation of the 1300-km-wide intracontinental orogen and postorogenic
1148 magmatic province in Mesozoic South China : A flat-slab subduction model. *Geology* 35, 179–
1149 182. <https://doi.org/10.1130/G23193A.1>
- 1150 Ligi, M., Bonatti, E., Bosworth, W., Cai, Y., Cipriani, A., Palmiotto, C., Ronca, S., Seyler, M., 2018. Birth
1151 of an ocean in the Red Sea: Oceanic-type basaltic melt intrusions precede continental rupture.
1152 *Gondwana Res.* 54, 150–160. <https://doi.org/10.1016/j.gr.2017.11.002>
- 1153 Ludwig, W.J., Nafe, J.E., Drake, C.L., 1970. Seismic refraction., in: Maxwell, A.E. (Ed.), *The Sea*. New-
1154 York, pp. 53–84.
- 1155 McKenzie, D., 1978. Some remarks on the formation of sedimentary basins. *Earth Planet. Sci. Lett.*
1156 40, 25–32.
- 1157 Mckenzie, D., Bickle, M.J., 1988. The volume and composition of melt generated by extension of the
1158 lithosphere. *J. Petrol.* 29, 1–55.
- 1159 Meyer, B., Saltus, R., Chulliat, A., 2017. EMAG2: Earth Magnetic Anomaly Grid (2-arc-minute
1160 resolution) Version 3. <https://doi.org/10.7289/V5H70CVX>
- 1161 Mohn, G., Karner, G.D., Manatschal, G., Johnson, C.A., 2015. Structural and stratigraphic evolution of
1162 the Iberia-Newfoundland hyper-extended rifted margin: a quantitative modelling approach.
1163 *Geol. Soc. London, Spec. Publ.* 15, 13810. <https://doi.org/10.1144/SP413.9>
- 1164 Morley, C.K., 2016. Major unconformities/termination of extension events and associated surfaces in
1165 the South China Seas: Review and implications for tectonic development. *J. Asian Earth Sci.* 120,
1166 62–86. <https://doi.org/10.1016/j.jseas.2016.01.013>
- 1167 Müller, R.D., Sdrolias, M., Gaina, C., Roest, W.R., 2008. Age, spreading rates, and spreading
1168 asymmetry of the world's ocean crust. *Geochemistry, Geophys. Geosystems* 9, 1–19.
1169 <https://doi.org/10.1029/2007GC001743>
- 1170 Müller, R.D., Seton, M., Zahirovic, S., Williams, S.E., Matthews, K.J., Wright, N.M., Shephard, G.E.,

- 1171 Maloney, K.T., Barnett-Moore, N., Hosseinpour, M., Bower, D.J., Cannon, J., 2016. Ocean Basin
1172 Evolution and Global-Scale Plate Reorganization Events Since Pangea Breakup. *Annu. Rev. Earth
1173 Planet. Sci.* 44, 107–138. <https://doi.org/10.1146/annurev-earth-060115-012211>
- 1174 Nagel, T.J., Buck, W.R., 2007. Control of rheological stratification on rifting geometry: A symmetric
1175 model resolving the upper plate paradox. *Int. J. Earth Sci.* 96, 1047–1057.
1176 <https://doi.org/10.1007/s00531-007-0195-x>
- 1177 Nanni, U., Pubellier, M., Chan, L.S., Sewell, R.J., 2017. Rifting and reactivation of a Cretaceous
1178 structural belt at the northern margin of the South China Sea. *J. Asian Earth Sci.* 136, 110–123.
1179 <https://doi.org/10.1016/j.jseaes.2017.01.008>
- 1180 Nirrengarten, M., Manatschal, G., Tugend, J., Kuszniir, N., Sauter, D., 2018. Kinematic evolution of the
1181 Southern North Atlantic: Implications for the formation of hyperextended rift systems.
1182 *Tectonics* 37, 89–118. <https://doi.org/10.1002/2017TC004495>
- 1183 Parker, R.L., 1972. The rapid calculation of potential anomalies, *Geophys J. R. astr. Soc.*, 31, 447–455
- 1184 Pérez-Gussinyé, M., Ranero, C.R., Reston, T.J., Sawyer, D., 2003. Mechanisms of extension at
1185 nonvolcanic margins: Evidence from the Galicia interior basin, west of Iberia. *J. Geophys. Res.*
1186 *Solid Earth* 108, 1–19. <https://doi.org/10.1029/2001JB000901>
- 1187 Peron-Pinvidic, G., Manatschal, G., Osmundsen, P.T., 2013. Structural comparison of archetypal
1188 Atlantic rifted margins: A review of observations and concepts. *Mar. Pet. Geol.* 43, 21–47.
1189 <https://doi.org/10.1016/j.marpetgeo.2013.02.002>
- 1190 Petri, B., Duretz, T., Mohn, G., Schmalholz, S.M., Karner, G.D., Müntener, O., 2019. Thinning
1191 mechanisms of heterogeneous continental lithosphere. *Earth Planet. Sci. Lett.* 512, 147–162.
1192 <https://doi.org/10.1016/j.epsl.2019.02.007>
- 1193 Pichot, T., Delescluse, M., Chamot-Rooke, N., Pubellier, M., Qiu, Y., Meresse, F., Sun, G., Savva, D.,
1194 Wong, K.P., Watremez, L., Auxiètre, J.L., 2014. Deep crustal structure of the conjugate margins
1195 of the SW South China Sea from wide-angle refraction seismic data. *Mar. Pet. Geol.* 58, 627–
1196 643. <https://doi.org/10.1016/j.marpetgeo.2013.10.008>
- 1197 Pin, Y., Di, Z., Zhaoshu, L., 2001. A crustal structure profile across the northern continental margin of
1198 the South China Sea. *Tectonophysics* 338.
- 1199 Pubellier, M., Ali, J., Monnier, C., 2003. Cenozoic Plate interaction of the Australia and Philippine Sea
1200 Plates: “hit-and-run” tectonics. *Tectonophysics* 363, 181–199. [https://doi.org/10.1016/S0040-1951\(02\)00671-6](https://doi.org/10.1016/S0040-1951(02)00671-6)
- 1202 Pubellier, M., Meresse, F., 2013. Phanerozoic growth of Asia: Geodynamic processes and evolution. *J.*
1203 *Asian Earth Sci.* 72, 118–128. <https://doi.org/10.1016/j.jseaes.2012.06.013>
- 1204 Pubellier, M., D. Savva, M. Aurelio, F. Sapin, 2017 Structural Map of the South China Sea, CCGM-
1205 CGMW [doi:10.14682/2017STRUCTUSCS](https://doi.org/10.14682/2017STRUCTUSCS)
- 1206 Reston, T.J., 2009. The structure, evolution and symmetry of the magma-poor rifted margins of the
1207 North and Central Atlantic: A synthesis. *Tectonophysics* 468, 6–27.
1208 <https://doi.org/10.1016/j.tecto.2008.09.002>
- 1209 Ru, K., Pigott, J.D., 1986. Episodic rifting and subsidence in the South China Sea. *Am. Assoc. Pet. Geol.*
1210 *Bull.* 70, 1136–1155. <https://doi.org/10.1306/94886A8D-1704-11D7-8645000102C1865D>
- 1211 Sandwell, D.T., Müller, R.D., Smith, W.H.F., Garcia, E., Francis, R., 2014. New global marine gravity
1212 model from CryoSat-2 and Jason-1 reveals buried tectonic structure. *Science* (80-.). 346, 65–67.
1213 <https://doi.org/10.1126/science.1258213>

- 1214 Savva, D., Pubellier, M., Franke, D., Chamot-Rooke, N., Meresse, F., Steuer, S., Auxietre, J.L., 2014.
1215 Different expressions of rifting on the South China Sea margins. *Mar. Pet. Geol.* 58, 579–598.
1216 <https://doi.org/10.1016/j.marpetgeo.2014.05.023>
- 1217 Schlüter, H.U., Hinz, K., Block, M., 1996. Tectono-stratigraphic terranes and detachment faulting of
1218 the South China Sea and Sulu Sea. *Mar. Geol.* 130, 39–78. [https://doi.org/10.1016/0025-](https://doi.org/10.1016/0025-3227(95)00137-9)
1219 [3227\(95\)00137-9](https://doi.org/10.1016/0025-3227(95)00137-9)
- 1220 Sclater, J.G., Jaupart, C., Galson, D., 1980. The heat flow through oceanic and continental crust and
1221 the heat loss of the Earth. *Rev. Geophys.* 18, 269–311.
1222 <https://doi.org/10.1029/RG018i001p00269>
- 1223 Seton, M., Whittaker, J.M., Wessel, P., Müller, R.D., DeMets, C., Merkouriev, S., Cande, S., Gaina, C.,
1224 Eagles, G., Granot, R., Stock, J., Wright, N., Williams, S.E., 2014. Community infrastructure and
1225 repository for marine magnetic identifications. *Geochemistry, Geophys. Geosystems* 15, 1629–
1226 1641. <https://doi.org/10.1002/2013GC005176>
- 1227 Sibuet, J.C., Yeh, Y.C., Lee, C.S., 2016. Geodynamics of the South China Sea. *Tectonophysics* 692, 98–
1228 119. <https://doi.org/10.1016/j.tecto.2016.02.022>
- 1229 Sizhong, P., Cunmin, C., 1993. Geology and geochemistry of source rocks of the Eastern Pearl River
1230 Mouth Basin, South China Sea. *J. Southeast Asian Earth Sci.* 8, 393–406.
1231 [https://doi.org/10.1016/0743-9547\(93\)90041-M](https://doi.org/10.1016/0743-9547(93)90041-M)
- 1232 Smith, R.A., 1961. A uniqueness theorem concerning gravity fields, *Proc. Cambridge Philos. Soc.*, 57,
1233 865–70
- 1234 Stein, S., Melosh, H.J., Minster, J.B., 1977. Ridge migration and asymmetric sea-floor spreading. *Earth*
1235 *Planet. Sci. Lett.* 36, 51–62. [https://doi.org/10.1016/0012-821X\(77\)90187-X](https://doi.org/10.1016/0012-821X(77)90187-X)
- 1236 Steuer, S., Franke, D., Meresse, F., Savva, D., Pubellier, M., Auxietre, J.L., Aurelio, M., 2013. Time
1237 constraints on the evolution of southern Palawan Island, Philippines from onshore and offshore
1238 correlation of Miocene limestones. *J. Asian Earth Sci.* 76, 412–427.
1239 <https://doi.org/10.1016/j.jseaes.2013.01.007>
- 1240 Stock, J.M., Sun, Z., Klaus, A., Larsen, H.C., Jian, Z., Alvarez Zarikian, C.A., Boaga, J., Bowden, S.A.,
1241 Briaies, A., Chen, Y., Cukur, D., Dadd, K.A., Ding, W., Dorais, M.J., Ferré, E.C., Ferreira, F.,
1242 Furusawa, A., Gewecke, A.J., Hinojosa, J.L., Höfig, T.W., Hsiung, K.H., Huang, B., Huang, E.,
1243 Huang, X.L., Jiang, S., Jin, H., Johnson, B.G., Kurzawski, R.M., Lei, C., Li, B., Li, L., Li, Y., Lin, J., Liu,
1244 C., Liu, C., Liu, Z., Luna, A., Lupi, C., McCarthy, A.J., Mohn, G., Ningthoujam, L.S., Nirrengarten,
1245 M., Osono, N., Peate, D.W., Persaud, P., Qiu, N., Robinson, C.M., Satolli, S., Sauermilch, I.,
1246 Schindlbeck, J.C., Skinner, S.M., Straub, S.M., Su, X., Tian, L., van der Zwan, F.M., Wan, S., Wu,
1247 H., Xiang, R., Yadav, R., Yi, L., Zhang, C., Zhang, J., Zhang, Y., Zhao, N., Zhong, G., Zhong, L., 2018.
1248 Site U1500, in: *Proceedings of the International Ocean Discovery Program Volume 367/368.*
1249 <https://doi.org/10.14379/iodp.proc.367368.104.2018>
- 1250 Sun, Z., Stock, J.M., Klaus, A., Larsen, H.C., Jian, Z., Alvarez Zarikian, C.A., Boaga, J., Bowden, S.A.,
1251 Briaies, A., Chen, Y., Cukur, D., Dadd, K.A., Ding, W., Dorais, M.J., Ferré, E.C., Ferreira, F.,
1252 Furusawa, A., Gewecke, A.J., Hinojosa, J.L., Höfig, T.W., Hsiung, K.H., Huang, B., Huang, E.,
1253 Huang, X.L., Jiang, S., Jin, H., Johnson, B.G., Kurzawski, R.M., Lei, C., Li, B., Li, L., Li, Y., Lin, J., Liu,
1254 C., Liu, C., Liu, Z., Luna, A., Lupi, C., McCarthy, A.J., Mohn, G., Ningthoujam, L.S., Nirrengarten,
1255 M., Osono, N., Peate, D.W., Persaud, P., Qiu, N., Robinson, C.M., Satolli, S., Sauermilch, I.,
1256 Schindlbeck, J.C., Skinner, S.M., Straub, S.M., Su, X., Tian, L., van der Zwan, F.M., Wan, S., Wu,
1257 H., Xiang, R., Yadav, R., Yi, L., Zhang, C., Zhang, J., Zhang, Y., Zhao, N., Zhong, G., Zhong, L., 2018.
1258 Site U1499, in: *Proceedings of the International Ocean Discovery Program Volume 367/368.*
1259 <https://doi.org/10.14379/iodp.proc.367368.103.2018>

- 1260 Taylor, B., Goodliffe, A.M., Martinez, F., 1999. How continents break up: Insights from Papua New
1261 Guinea. *J. Geophys. Res.* 104, 7497. <https://doi.org/10.1029/1998JB900115>
- 1262 Taylor, B., Hayes, D., 1983. Origin and history of the South China Sea basin, in: Hayes, D. (Ed.), *The*
1263 *Tectonic and Geologic Evolution of Southeast Asian Seas and Islands: Part 2.* pp. 23–56.
- 1264 Tugend, J., Manatschal, G., Kuszniir, N.J., Masini, E., 2015. Characterizing and identifying structural
1265 domains at rifted continental margins: application to the Bay of Biscay margins and its Western
1266 Pyrenean fossil remnants. *Geol. Soc. London, Spec. Publ.* 413, 171–203.
1267 <https://doi.org/10.1144/SP413.3>
- 1268 Tucholke, B.E., Sawyer, D.S., Sibuet, J.-C., 2007. Breakup of the Newfoundland–Iberia rift. *Geol. Soc.*
1269 *London, Spec. Publ.* 282, 9–46. <https://doi.org/10.1144/SP282.2>
- 1270 Tucholke, B.E., Sibuet, J.-C., 2007. Leg 210 Synthesis: Tectonic, Magmatic, and Sedimentary Evolution
1271 of the Newfoundland–Iberia Rift, in: *Proceedings of the Ocean Drilling Program, 210 Scientific*
1272 *Results.* <https://doi.org/10.2973/odp.proc.sr.210.101.2007>
- 1273 Wang, J., Pang, X., Liu, B., Zheng, J., Wang, H., 2018. The Baiyun and Liwan Sags: Two
1274 supradetachment basins on the passive continental margin of the northern South China Sea.
1275 *Mar. Pet. Geol.* 95, 206–218. <https://doi.org/10.1016/j.marpetgeo.2018.05.001>
- 1276 Wang, P., Prell, W.L., Blum, P., 2000. Leg 184 Summary: Exploring the Asian Monsoon through Drilling
1277 in the South China Sea, in: *Proceedings of the Ocean Drilling Program, 184 Initial Reports,*
1278 *Proceedings of the Ocean Drilling Program. Ocean Drilling Program.*
1279 <https://doi.org/10.2973/odp.proc.ir.184.101.2000>
- 1280 Wang, T.K., Chen, M.K., Lee, C.S., Xia, K., 2006. Seismic imaging of the transitional crust across the
1281 northeastern margin of the South China Sea. *Tectonophysics* 412, 237–254.
1282 <https://doi.org/10.1016/j.tecto.2005.10.039>
- 1283 Whitmarsh, R.B., Manatschal, G., Minshull, T.A., 2001. Evolution of magma-poor continental margins
1284 from rifting to seafloor spreading. *Nature* 413, 150–154. <https://doi.org/10.1038/35093085>
- 1285 Whitmarsh, R.B., Sawyer, D.S., Klaus, A., Masson, D.G. (Eds.), 1996. *Proceedings of the Ocean Drilling*
1286 *Program, 149 Scientific Results, Proceedings of the Ocean Drilling Program. Ocean Drilling*
1287 *Program.* <https://doi.org/10.2973/odp.proc.sr.149.1996>
- 1288 Whitmarsh, R.B., Wallace, P.J., 2001. *Proceedings of the Ocean Drilling Program, 173 Scientific*
1289 *Results 173.* <https://doi.org/10.2973/odp.proc.sr.173.2001>
- 1290 Whittaker, J.M., Goncharov, A., Williams, S.E., Müller, R.D., Leitchenkov, G., 2013. Global sediment
1291 thickness data set updated for the Australian–Antarctic Southern Ocean. *Geochemistry,*
1292 *Geophys. Geosystems* 14, 3297–3305. <https://doi.org/10.1002/ggge.20181>
- 1293 Williams, H.H., 1997. Play concepts–northwest Palawan, Philippines. *J. Asian Earth Sci.* 15, 251–273.
1294 [https://doi.org/10.1016/S0743-9547\(97\)00011-1](https://doi.org/10.1016/S0743-9547(97)00011-1)
- 1295 Xia, S., Liu, Z., Luo, D., Shu, L., Zhang, Z., Gao, L., Dong, G., Zhang, L., Leng, C., Zhang, B., 2018.
1296 Sequence architecture and depositional evolution in Lufeng Depression, Pearl River Mouth
1297 Basin, South China Sea Part A: The braided delta deposits of Cenozoic Enping Formation. *Geol. J.*
1298 <https://doi.org/10.1002/gj.3117>
- 1299 Yang, L., Ren, J., McIntosh, K., Pang, X., Chao, L., Zhao, Y., 2018. The structure and evolution of
1300 deepwater basins in the distal margin of the northern South China Sea and their implications for
1301 the formation of the continental margin. *Mar. Pet. Geol.* 92, 234–254.
1302 <https://doi.org/10.1016/j.marpetgeo.2018.02.032>

- 1303 Ye, Q., Mei, L., Shi, H., Shu, Y., Camanni, G., Wu, J., 2018. A low-angle normal fault and basement
1304 structures within the Enping Sag, Pearl River Mouth Basin: Insights into late Mesozoic to early
1305 Cenozoic tectonic evolution of the South China Sea area. *Tectonophysics* 731–732, 1–16.
1306 <https://doi.org/10.1016/j.tecto.2018.03.003>
- 1307 Zahirovic, S., Seton, M., Müller, R.D., 2014. The Cretaceous and Cenozoic tectonic evolution of
1308 Southeast Asia. *Solid Earth* 5, 227–273. <https://doi.org/10.5194/se-5-227-2014>
- 1309 Zhang, C., Su, M., Pang, X., Zheng, J., Liu, B., Sun, Z., Manatschal, G., 2019. Tectono-Sedimentary
1310 Analysis of the Hyperextended Liwan Sag Basin (Midnorthern Margin of the South China Sea).
1311 *Tectonics*. <https://doi.org/10.1029/2018TC005063>
- 1312 Zhao, M., Qiu, X., Xia, S., Xu, H., Wang, P., Wang, T.K., Lee, C.S., Xia, K., 2010. Seismic structure in the
1313 northeastern South China Sea: S-wave velocity and Vp/Vs ratios derived from three-component
1314 OBS data. *Tectonophysics* 480, 183–197. <https://doi.org/10.1016/j.tecto.2009.10.004>
- 1315 Zhou, D., Ru, K., Chen, H., 1995. Kinematics of Cenozoic extension on the South China Sea continental
1316 margin and its implications for the tectonic evolution of the region. *Tectonophysics* 251, 161–
1317 177. [https://doi.org/10.1016/0040-1951\(95\)00018-6](https://doi.org/10.1016/0040-1951(95)00018-6)
- 1318 Zhou, Z., Mei, L., Liu, J., Zheng, J., Chen, L., Hao, S., 2018. Continentward-dipping detachment fault
1319 system and asymmetric rift structure of the Baiyun Sag, northern South China Sea.
1320 *Tectonophysics* 726, 121–136. <https://doi.org/10.1016/j.tecto.2018.02.002>
- 1321
- 1322